CHAPTER

5

Temperature Rise at the Tip of Dynamically Propagating Cracks: Measurements Using High-Speed Infrared Detectors

Alan T. Zehnder

Department of Theoretical and Applied Mechanics
Cornell University, Ithaca, NY 14853-1503

Ares J. Rosakis

Graduate Aeronautical Laboratories
California Institute of Technology, Pasadena, CA 91125

During dynamic crack growth, energy dissipated at the crack-tip causes a temperature increase. Although it has been recognized for many years that the temperature rise may have a strong influence on the dynamic fracture toughness of a material, until recently no means were available for a direct experimental measurement of the crack-tip temperature field. A technique is presented here that uses arrays of high-speed infrared detectors to measure of the distribution of temperature increase inside the crack-tip plastic zone. General aspects of infrared detectors, infrared optics, and potential applications of this technique are discussed. Results for a particular experimental measurement of temperature rise during dynamic crack growth in 4340 steel are also discussed.

Introduction

During any inelastic deformation of a material, work done on the material is either stored in the material or dissipated as heat or acoustic energy. The

majority of the energy is dissipated as heat [1,2], thus when a deformation occurs at a high enough rate, the heat cannot be dissipated as fast as it is generated, resulting in an increase in the temperature of the material. Higher temperatures generally "soften" a material, resulting in changes in the deformation fields that can lead to localization, fracture, or reduced strength of the structure containing the material. Examples of situations where thermal softening could be important include dynamic crack growth, high velocity impact, high-speed cutting, high-speed metal forming, and adiabatic shear band formation. Although the experimental techniques presented here will concentrate on applications to dynamic fracture, the concepts can be generalized to apply to any situation where temperature rise during dynamic deformation is important.

Despite the potential importance of crack-tip heating on dynamic fracture toughness, until very recently no attempt to directly measure the temperature at the tip of a truely dynamically growing crack in a metal had been made. However, recent advances in infrared detectors now make it possible to measure, in real time, the spatial distribution of crack-tip temperature for dynamically propagating cracks.

We first discuss the problems of temperature rise during dynamic crack growth and review both experimental and theoretical work done in this area. Next infrared detectors and their use for performing temperature measurements are discussed. In the last section an application of an array of high-speed infrared detectors to the measurement of crack-tip temperature in 4340 steel is presented. The goal of the experiments described here is to directly measure the temperature fields at the tips of dynamically propagating cracks, to use this information to study the energy flows to the crack-tip and to infer the influence of crack-tip heating on the dynamic fracture process. The concept of the experiment is as follows: A linear array of high-speed infrared (IR) detectors is used to measure the temperature at discreet points covering a line segment perpendicular to and intersecting the path of a dynamically propagating crack. As the crack traverses the line segment, the voltage outputs from each of the detector elements are recorded simultaneously on a set of digital oscilloscopes. At the same time the crack length record is measured using a conductive grid technique. Knowing the temperature versus time at the observation points and using the measured crack length versus time record, the temperature distribution near the crack-tip is found.

Temperature Rise During Dynamic Crack Growth

Consider a Mode-I crack propagating dynamically with an instantaneous crack length $a(t)$, and speed $\dot{a}(t)$, as shown in Fig. 5.1. As the crack approaches a material particle on $x_2 = 0$, the particle is loaded first elastically, and then plastically within the active crack-tip plastic zone, defined as the

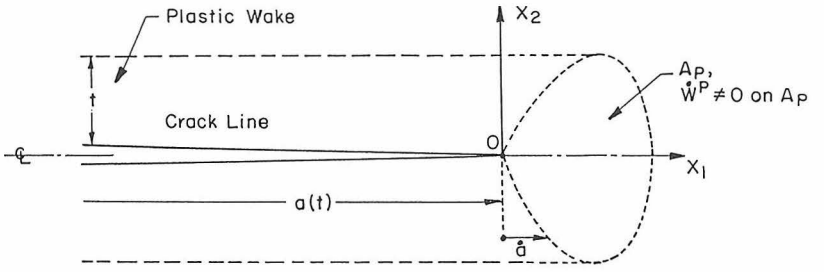

Figure 5.1. Active plastic zone and wake for Mode-I dynamic crack growth.

region where the plastic work rate $\dot{W}^P$ is positive. When the crack-tip reaches the material particle, the particle is fractured and then unloads elastically and enters the wake region. During the initial elastic loading there is a very small thermoelastic cooling due to the volume dilation, followed by heating during the plastic loading. The particle rapidly heats up to its maximum temperature and then slowly cools down by conduction after the crack passes. The time t_0 for the particle to reach its maximum temperature is the time it takes for the particle to go from the onset of plastic deformation to fracture. In terms of $\dot{a}$ and plastic zone size r_p the time is $t_0 = r_p/\dot{a} \approx 2$ μs, estimating $r_p \approx 2$ mm and $\dot{a} \approx 1$ mm/μs. After the crack passes and the material is in the plastic wake no further heating occurs.

For an elastic-plastic, isotropic, homogeneous material with constant thermal conductivity, the heat conduction equation can be written as

$$k\nabla^2\Theta - \alpha(3\lambda + 2\mu)\Theta_0\dot{\varepsilon}_{\kappa\kappa} + \eta\sigma_{ij}\dot{\varepsilon}^P_{ij} = \dot{\rho}c\Theta, \tag{1}$$

where k is the thermal conductivity, Θ is the absolute temperature, α is the coefficient of thermal expansion, λ and μ are elastic constants, Θ_0 is the initial temperature, ε_{ij} and σ_{ij} are the Cartesian components of the strain and stress tensors, ρ is the density, and c is the specific heat. The quantity η is the fraction of plastic work rate density, $\dot{W}^P = \sigma_{ij}\dot{\varepsilon}^P_{ij}$, dissipated as heat. In general η is not a constant but is a function of plastic strain, strain rate, and possibly other variables [3]. However, data [1,2] indicate that η is usually between 0.9 and 1.0. The solution to Eq. (1) involves integrals over time and over the active plastic zone [4]. Thus if the distribution of the plastic work rate density $\dot{W}^P$ is known from an analytical or a numerical model of the crack growth problem, then the temperature distribution around the crack-tip can be calculated. This is exactly the approach taken by a number of theoretical investigations on the subject, some of which are outlined below.

In an early investigation by Rice and Levy [5], the crack-tip field is approximated by a Dugdale line plastic zone model. The resulting calculation allows the maximum temperature increase $(\Theta - \Theta_0)_{max} \equiv T_{max}$, to be calculated given the stress intensity factor K^d_I, the crack speed $\dot{a}$, the yield stress,

and the thermal properties of the material. They found that T_{max} increases with increasing K_I^d and increasing $\dot{a}$. For properties typical of mild steel, T_{max} is approximately 200 °C, while for titanium (which has a much lower conductivity) $T_{max} \approx 500$ °C. In Weichert and Schönert [6] the plastic work was assumed to be spread uniformly over a circular or rectangular region propagating with the crack-tip. By estimating the energy release rate and the area over which the heating occurs, they predicted temperatures well in excess of 3000 °C for brittle materials such as glass and quartz.

In finite element calculations for the crack-tip temperature rise, Kuang and Atluri [7] distributed the heating due to plastic work uniformly and in a $1/r$ distribution, where r is the distance from the crack-tip. They estimated $T_{max} \approx 1000$ °C for a crack propagating at high speed. Malali [8] used finite elements to solve for $\dot{W}_p$ for Mode-III (antiplane shear) dynamic crack growth in an elastic perfectly plastic material. In this solution $T_{max} \approx 240$ °C for steel and is approximately 4000 °C for a titanium alloy.

A recent finite element calculation by Krishnakumar, Narasimhan, and Prabhaker [9] simulated plane strain, steady state, and dynamic crack growth in a viscoplastic material. Using the plastic work rate distribution calculated from the finite element model, and assuming that all of the work is dissipated as heat, they calculated the resulting temperature rise near the crack-tip to be 160–240 °C, depending on crack growth speed and on material properties.

Simulating crack growth in an elastic-viscoplastic, porous metal, Needleman and Tvergaard [10] used finite elements to calculate the deformation fields and temperature rise due to dynamic crack growth in a double edge cracked specimen. Their calculation, which couples the temperature rise, material constitutive properties and the deformation fields, predicts maximum temperature rises of ≈100 °C.

Care must be taken in interpreting any of the above results since they are very sensitive to the constitutive law, to whether the calculation assumes plane strain, plane stress, or anitiplane shear kinematics, and on the choice of material parameters, which are not always realistic. For example, it is unlikely that a ductile steel with a low yield stress can sustain crack growth at speeds of 1000 m/s, as assumed in some analyses. Work in progress by Rosakis and Deng [11], who are modeling plane stress, Mode-I crack growth, should provide more realistic estimates.

Several authors have used infrared (IR) detectors to study problems in solid mechanics. A copper-doped germanium detector was used by Moss and Pond [12] to study the heat generated by discontinuous yielding in copper. In their experiment radiation was collected onto the detector with a spherical mirror system and the resulting signals were recorded dynamically. Since a single element detector was used, no attempt was made to produce an image of the temperature field.

The first experiments to use a *focused,* imaging system of IR detectors for a truly dynamic experiment are those of Duffy and co-workers [13,14].

They used a linear array of indium antimonide (InSb) detectors focused on a specimen undergoing dynamic shear loading. The dynamic shear band formed in their experiments is a source of heat causing the temperature to rise 400 °C in 50 μs. It was found that this heating is critical in producing thermal softening, leading to deformation instability.

IR detectors have even been used to study stress wave reflections, by measuring the very small temperature changes produced by the thermoelastic effect in stress waves [15]. In this work a low-speed, pyroelectric, thermal detector was used. Thermal cameras, which typically scan their field of view in 1/30 s, have been used in numerous quasistatic experiments. For example, thermal cameras are applied for a stress analysis technique known as SPATE [16] (stress pattern analysis by thermal emissions) that measures the temperature due to thermoelastic heating and cooling of a body under cyclic loading. Note, however, that thermal cameras are much too slow to measure the temperature at the tip of a dynamically propagating crack.

Most of the experimental measurements of temperature in dynamic fracture have concentrated on measuring the energy release rate or the maximum temperature at the crack-tip. In the work by Fuller, Fox, and Field [17], a number of experimental techniques were combined to study crack-tip heating. A single element, unfocused, IR detector system was used to measure the maximum temperature at the tip of a dynamic crack in PMMA. The maximum temperature recorded is 500 °C. In addition, thermocouples and a liquid crystal film deposited on the specimen surface were also used to estimate the total heat dissipated during crack growth.

In the work by Weichert and Schönert [6], an unfocused high-speed infrared spectrometer was used to measure peak temperature during the fragmentation of a glass plate. In addition, they used thermistors to estimate total heat generation during crack growth.

In recent work by Shockey et al. [18], thermocouples of 25–50 μm dimensions are welded to the surface of the test specimen near the prospective crack path. As the crack propagates past the thermocouples the temperature is recorded. Typically the temperatures measured are less than 1 °C since the thermocouples are located greater than 1 mm from the crack path, where the heating actually occurred. By treating the crack as a one-dimensional heat source that instantaneously delivers a heat flux all along the crack line at the same time, the magnitude of this heat flux can be computed from the measured temperature. In this way an estimate of the energy release rate, G, can be obtained. Values obtained for G are within a factor of 2 of the value obtained from $G \approx K_I^2/E$ (energy release rate for quasistatic crack growth in elastic materials), where K_I is the stress intensity factor and E is Young's modulus.

Other experimental measurements of near-tip temperatures are presented by Döll [19], Tomashevskii, Egorov, and Sovodstin [20], Fox and Soria-Ruiz [21], and Kobayashi et al. [22] while a metallurgical study presenting evidence of local melting in two titanium alloys is presented in Bryant, Makel,

and Wilsdorf [23]. Klemm [24] studied fast crack growth in highly ductile pipeline steels (crack velocities up to 80 m/s), using a series of thermocouples. Temperature profiles across a 50 mm radius plastic zone were recorded with a maximum temperature increase of approximately 100 °C. In addition to studies of temperature rise during fracture, a number of researchers have measured temperature rise during low cycle fatigue, relating the energy dissipation to damage in the material [25,26].

Infrared Systems for Dynamic Fracture

Electromagnetic radiation is constantly emitted from bodies that are at temperatures greater than absolute zero. Since the radiant flux E emitted per unit area is $E = \varepsilon\sigma\Theta^4$, where ε is the total emissivity of the body, σ is the Stephan–Boltzman constant, $\sigma = 5.67 \times 10^{-12}$ $W/cm\ °K^4$, and Θ is the absolute temperature, measurement of the emitted radiation provides a sensitive measurement of the temperature of the body.

For problems involving high speed deformations of materials the temperatures to be measured are expected to range from room temperature up to the melting temperatures of materials. At such temperatures (300–2,000 $°K$) the emitted radiant energy is concentrated in the infrared range of wavelengths, 0.7–30 μm. Thus for mechanics experiments, interest is concentrated on detecting infrared radiation and on relating the measured radiation to the temperature of the emitting body.

Infrared Detector Choices

Many types of IR detectors are available commercially. The choice of detector type is dictated by the temperature range to be measured, by the rate of change of temperature, by the size of the region where the temperature change will occur, and by whether a point or a field measurement is required. There are two basic types of detectors, thermal detectors that heat or cool due to radiation incident upon them, and photon detectors that remain at constant temperature but respond to photons incident upon the detector.

Thermal Detectors

Thermal detectors absorb the radiant energy focussed onto them, causing a change in the temperature of the detector element. This results in a measurable change in the electrical properties of the element. The elements are made of either pyroelectric materials, thermistors, or thermopiles. Pyroelec-

tric materials produce an electrical charge when the temperature is changed, thermistors change their electrical resistance due to temperature changes and thermopiles are essentially a series of thermocouples that produce a voltage proportional to the temperature. Thermal detectors can be made to absorb radiation from all wavelengths, thus they are useful for measuring temperature over an almost unlimited range. They are also generally inexpensive, mechanically rugged, do not require cryogenic cooling and can be made into one- or two-dimensional arrays. However, due to the finite amount of time required to heat or cool the detector elements, they are relatively slow in their time response [27]. The fastest of these devices appear to have minimum rise times of 10 μs.

Photon Detectors

Photon detectors are semiconductor devices that produce charge carriers when excited by photons having energies within a range that depends on the particular semiconductor being used. This implies that the detector element responds to radiation within a range of wavelengths, since the energy e of a photon is $e = hc/\lambda$, where λ is the wavelength, c is the speed of light, and h is Planck's constant. These devices are either photoconductive, where a fixed voltage is maintained across the device and the current varies as the number of charge carriers varies, or photovoltaic devices where the voltage across a p-n junction changes. In either case, photon detectors have the advantages of very fast response time (down to nanoseconds) and sensitivity that is orders of magnitude greater than thermal detectors. They can be made quite small (100 μm size elements are not unusual) and are available as single elements on in linear or two-dimensional arrays. Their disadvantages are that they are sensitive only to a fixed range of wavelengths of radiation, generally require cryogenic cooling, and are relatively expensive.

A wide variety of photoconductive and photovoltaic photon detectors are available. The choice of detector element material depends primarily on the range of temperature (and hence wavelength range of emitted radiation) to be measured. The spectral distribution of blackbody radiation is given by Planck's equation

$$P(\lambda, \Theta) = \frac{C_1}{\lambda^5(e^{c_2/\lambda\Theta} - 1)}, \tag{2}$$

where $P(\lambda, \Theta)$ is the radiant power emitted per unit area, per unit wavelength, $C_1 = 37{,}404\ W(\mu m)^4/cm^2$, and $C_2 = 14{,}387\ \mu m\ ^\circ K$. $P(\lambda, \Theta)$ is shown in Fig. 5.2 along with the spectral responsivities of several common IR detector materials. A detector is chosen such that its responsivity overlaps the emitted radiation as much as possible for the range of temperatures expected.

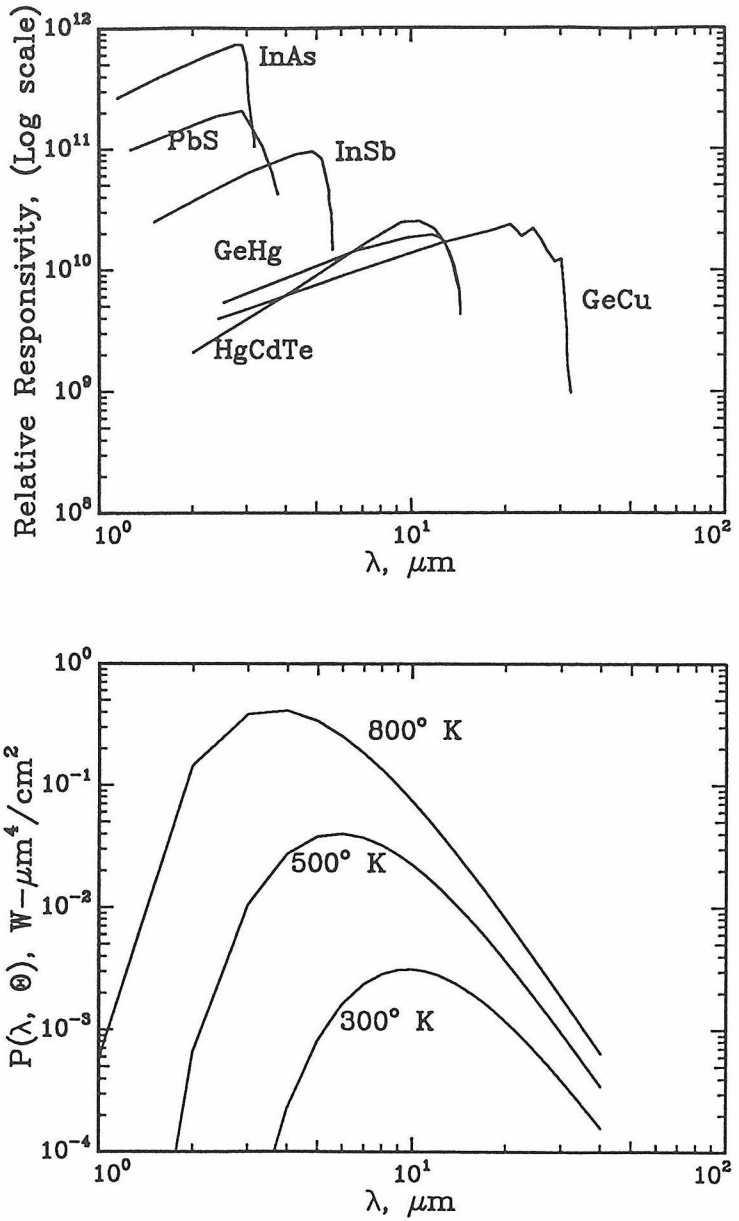

Figure 5.2. Spectral responsivity of several common photon detectors and the blackbody spectral radiation at various temperatures.

Points versus Field Measurements

Thermal or photon detectors can be used in a variety of applications that include point or field measurements. To measure the temperature of a point or small area, all that is required is a single element focussed on the object being investigated. To measure a temperature *field* either a scanning system or an array of detectors is required.

Commercially available infrared video cameras use a single detector or a linear array of detectors that are scanned over the required field of view using a system of rotating mirrors. These cameras can typically record a single frame in video camera speed, 1/30 s. Many cameras also have a fast line scan mode where a single line can be scanned and recorded in less than 1 ms, which is still too slow for dynamic fracture applications.

A one- or two-dimensional array of detectors can be used without scanning to measure the distribution over one- or two-dimensional fields of view. Such systems have the potential of much higher speed than the scanning devices since the signals from each detector element can be recorded simultaneously. However, they will be relatively expensive since each detector element requires a separate amplifier and data recorder, each operating in parallel.

Detector Speed and Sensitivity

In most cases, the time response of the detector is limited not by the detector element, but by the electronics associated with it. The circuit for preamplifying the output of a typical photovoltaic detector element consists of a transimpedence amplifier as shown in Fig. 5.3 [28]. The detector, which operates as a photodiode, produces a current that is amplified and converted to a voltage by the circuit. The detector is modeled as a perfect current source (this includes noise and signal currents) with a capacitance C_D and resistance R_D in parallel. The amplification A of this circuit defined as $A = V_0/i_D$, where V_0 is the output voltage and i_D is the detector current, is [28]

$$A = \frac{-R_f}{(1 + j2\pi f R_f C_f) + \dfrac{1}{A_0}\dfrac{R_f}{R_d}(1 + j2\pi f R_D C_D)}, \tag{3}$$

where A_0 is the open loop gain of the operational amplifier, f is the frequency, R_f is the feedback resistance, and C_f is the feedback capacitance. Equation (3) shows that at low frequencies $A \sim R_f$, thus a larger R_f increases the sensitivity of the system. However, for high-speed applications the frequency response of the system must be considered. The frequency dependence of $|A/R_f|$ is plotted in Fig. 5.4 for various values of R_f, assuming the following typical values for the circuit parameters: $A_0 = 500$, $C_D = 7$ pf, $R_f = 4 \times 10^{10}\Omega$, and $C_f = 0.4$ pf. It is seen that the amplification begins to decrease at lower frequencies for higher values of R_f. Since the bandwidth

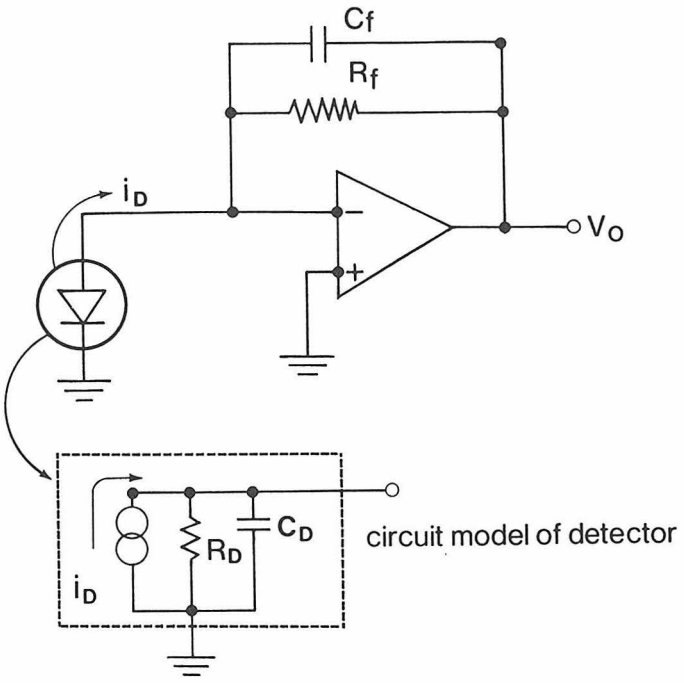

Figure 5.3. Preamplifier circuit for photovoltaic detectors, and circuit model of detectors [28].

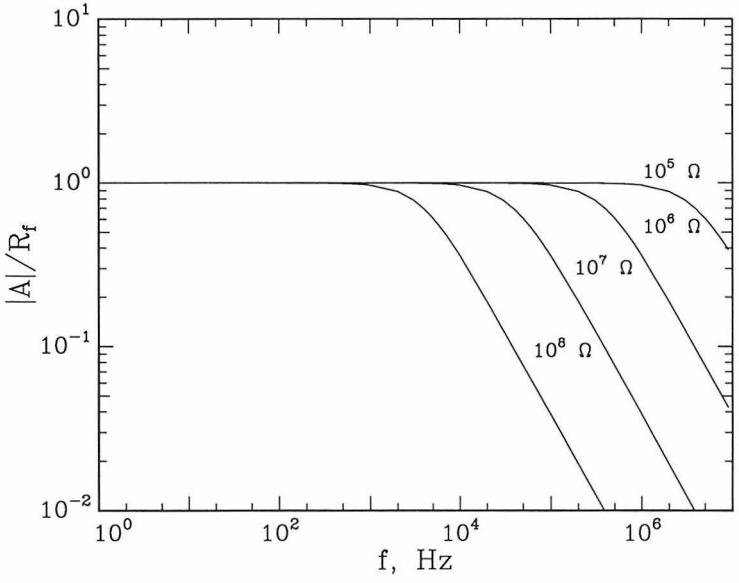

Figure 5.4. Frequency response for photovoltaic detector circuit with various values of feedback resistance R_f.

decreases with increasing R_f, but overall amplification increases with R_f, there is a tradeoff to be made between speed and sensitivity in choosing the detector electronics. Note that the frequency response cannot be extended indefinitely by continuing to lower R_f since instabilities will develop as R_f decreases, requiring increasing the capacitance C_f, which in turn lowers the bandwidth. Note also that many of the amplifiers are designed to be insensitive to dc signals, thus there is a low-frequency limitation as well. For dynamic applications this insensitivity is an advantage since the detectors will not respond to constant background radiation, which would tend to obscure the desired information.

Experimental measurements of the frequency response for a real detector system are shown in Figs. 5.5 and 5.6 for three values of R_f in the same detector. The detector, an array of .08 mm × .08 mm indium antimonide (InSb) elements from Cincinatti Electronics, was tested by placing an infrared light-emitting diode (IR-LED) in front of the detector and pulsing the IR-LED producing a 50 *ns* pulse of radiation. The output from the detectors due to this pulse is shown in Fig. 5.5. This output closely approximates the impulse response of the detector, and thus the fast Fourier transform (FFT) of the response to the IR-LED provides the frequency response curves, shown in Fig. 5.6 for various values of R_f. The tradeoff made in speed versus sensitivity is apparent in Fig. 5.6, where the output is higher for higher R_f, but the bandwidth is lower.

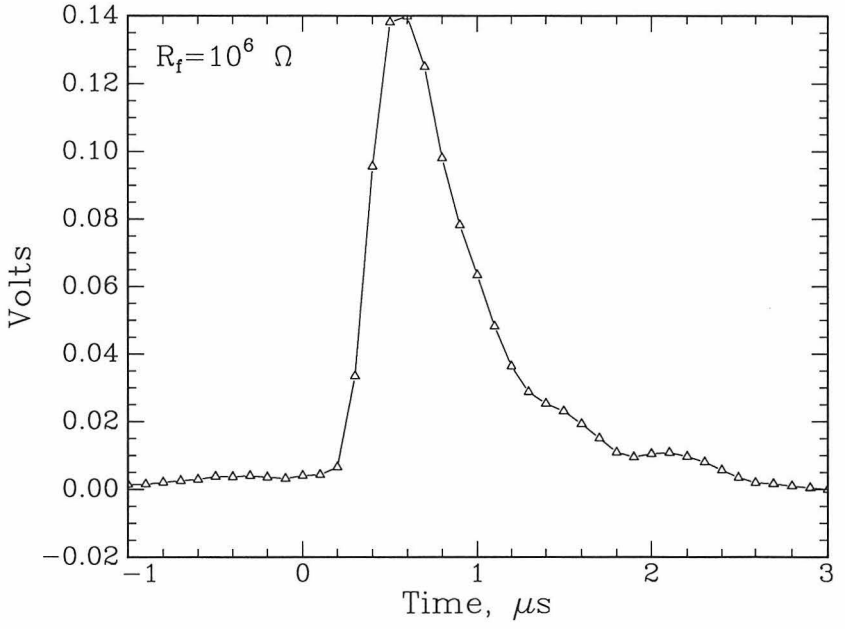

Figure 5.5. Measured response of an Indium Antimonide (InSb) detector to a 50 ns duration pulse of IR radiation.

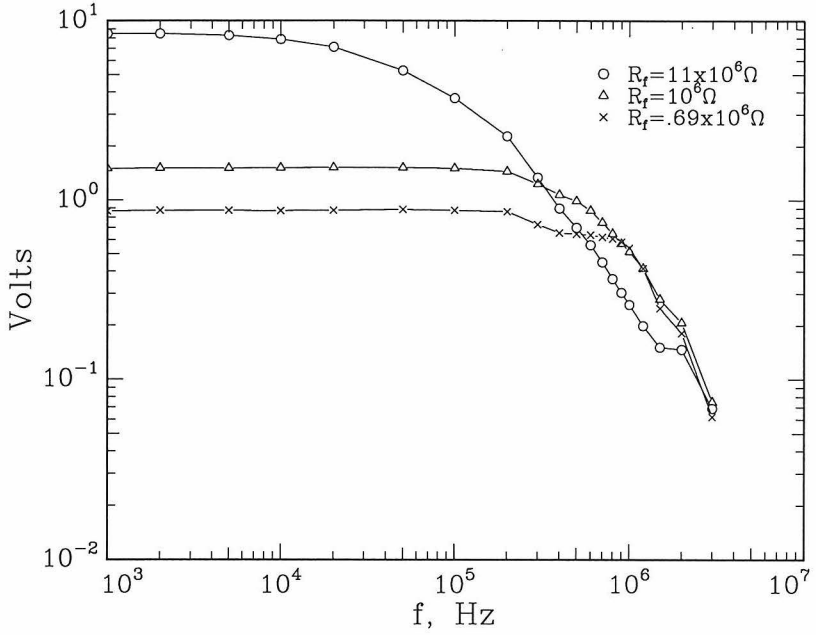

Figure 5.6. Measured frequency response of InSb detectors with various values of R_f.

Choosing the size of a detector element involves consideration of required spatial resolution, sensitivity and speed. A smaller element has a lower capacitance, C_D and hence higher potential speed. It will also provide finer spatial resolution since a single element can view a smaller area of the specimen. However, a smaller element will collect less radiation than a larger one, and will thus suffer a loss in sensitivity compared to a larger detector element.

Infrared Optics

Radiation is emitted from a surface in all directions. For a detector to measure this radiation, some means of bringing the radiation from the surface to the detector must be provided. Three possibilities, a focused system, an unfocused system, and an unfocused but collecting system are illustrated in Fig. 5.7.

If the detector is a multielement array, a focusing system allows for the measurement of the distribution of temperature over a specific small region. In the unfocused system, radiation from many points on the sample reaches a given point on the detector, thus there is no way to determine the distribution of temperature over the body. In a collecting system [12] a reflector is used to concentrate radiation onto the detector without necessarily focus-

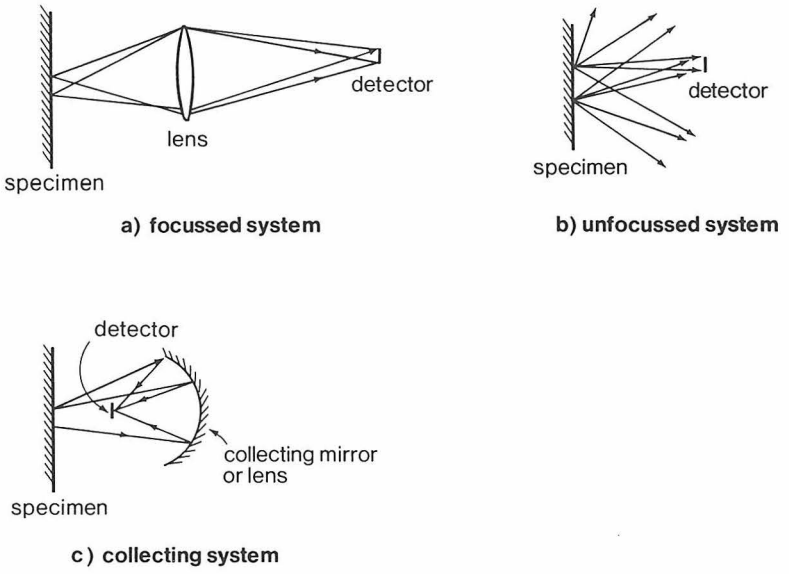

Figure 5.7. Types of optical systems used with infrared detectors. (a) Focused. (b) Unfocused. (c) Collecting.

ing. Such a system allows for the use of inexpensive optics while providing a large energy gathering capability. The unfocused systems are appropriate only when the temperature of the region to be measured is uniform or when an average temperature is required [6,17]. When it is required to measure spatial temperature distributions, focusing optics are necessary. The basic optical system types are either refractive, reflective, or combinations of the two (catadioptric).

Refractive Optics

A schematic of a refractive system is shown in Fig. 5.8. Just as in a visible light system, the lens must transmit the radiation from the object plane (the specimen) to the image plane (the detector) with a minimum of aberrations and a maximum of efficiency. Unlike visible light optics, lenses for infrared use cannot be made of glass since glass does not transmit infrared radiation. Commonly used infrared lens materials include Si, Ge, NaCl, ZnSe, and many others [28,29]. Unfortunately, most of these materials do not transmit visible light well, making it difficult to focus the optics by eye. The choice of lens material is primarily influenced by the wavelength range that will be measured. The lens must transmit well in this range and must have a sufficiently low dispersion (variation of refractive index with λ) to minimize chromatic aberration.

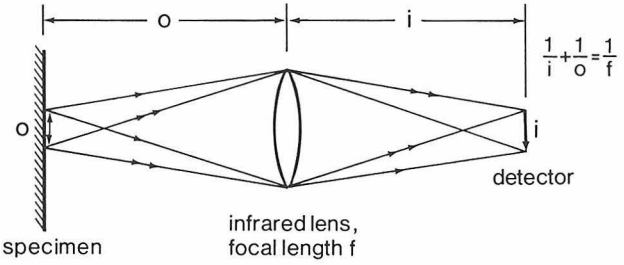

Figure 5.8. Refractive optical system.

The refractive systems have the advantages that a great number of component lenses and lens systems are available commercially, and the design allows for a straight optical path. The disadvantages of refractive IR lens systems are chromatic aberrations, limited useable wavelengths, the antireflection coatings required due to their high indices of refraction of IR lens materials, and their nontransparency to visible light.

Reflective Optics

Using reflective optics instead of refractive allows for the use of visible light to focus the system, eliminates the chromatic aberrations and provides a system useful over a much wider range of wavelengths. The only limitation on wavelength is that reflective coatings (gold, aluminum, silver) reflect some wavelengths better than others. The disadvantages of reflective optics are that the optical path is often folded, resulting in a complex layout of the components, and that there are very few commercially available systems or components.

The Offner system [30] shown in Fig. 5.9(a) is useful when imaging at a 1:1 magnification. It consists of two spherical mirrors located such that their centers of curvature are coincident. The radius of curvature of the larger,

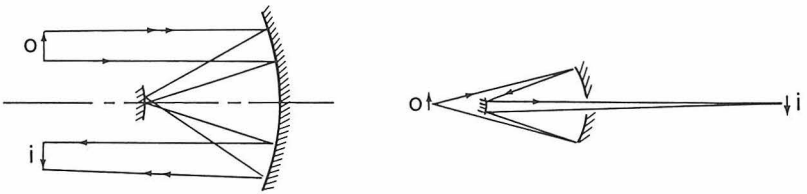

a) Offner mirror system **b) Schwarzschild objective**

Figure 5.9. Reflective optical systems. (a) Offner system. (b) Schwarzschild miscroscope objective.

concave mirror is twice that of the the smaller convex mirror. This mirror system eliminates spherical aberrations and due to the large size of the mirrors (relative to their curvatures) it has a large energy gathering capability.

The Schwarzschild objective shown in Fig. 5.9 is a reflective microscope objective that is available commercially [31] for 15×, 25×, 36×, 52×, and 74× magnifications. These systems have excellent imaging capabilities with zero spherical, coma, and astigmatic aberrations. The 15× system was used by Chrisman, Duffy, and Chi [14] in their work on dynamic shear band formation. For more information on infrared optics and on optical design in general see Refs. [28,32].

Data Processing

The complete experimental system must be considered to consist of the detector, amplifiers, data recorders (digital oscilloscopes or transient waveform recorders), and data processors (computer software). The output from the detector amplifiers will be a voltage record that must be interpreted to determine the temperature of the emitting body. The requirements for the digital oscilloscopes are the same as those for recording any transient signal. The sampling rate must be fast enough to record the highest frequencies of the signal, i.e., $\Delta t \leq 1/2f_{\max}$ where Δt is the time between points recorded, and $f_{\max}$ is the highest frequency contained in the the signal. The recoder resolution is dictated by the required precision in the results. Generally 8-bit resolution (1 in 256) is the acceptable minimum. A separate channel of data acquisition is required for each IR detector element and the memory length of the recorders must be sufficient to cover the entire time span of interest when sampling at the maximum rate. The recorder data, in the form of voltage versus time, can then be transferred to a computer for processing.

Calibration

Careful calibration of the system is crucial to obtain accurate results. In principle, the calibration can be performed either experimentally or analytically, however the difficulty in determining the parameters in the analytical expression makes a direct experimental calibration preferable.

Assuming an IR detector that is not sensitive to dc signals, the voltage output of a detector is governed by the *difference* between the radiation emitted due to any temperature *increase* (assumed to be of sufficiently high frequency to be amplified) and the dc signal due to the radiation emitted at *room temperature*,

$$V(\Theta, \Theta_0) = AA_D\beta \int_{\lambda_{min}}^{\lambda_{max}} R(\lambda)[P(\lambda, \Theta)\varepsilon(\lambda, \Theta) - P(\lambda, \Theta_0)\varepsilon(\lambda,\Theta_0)]\, d\lambda, \tag{4}$$

where Θ is the absolute temperature, Θ_0 is the room temperature, A is the amplification, A_D is the detector area, β is the fraction of energy emitted from the specimen that is transmitted to the detectors ($\beta < 1$), $\varepsilon(\lambda, \Theta)$ is the emissivity of the emitting body at wavelength λ and absolute temperature Θ, $R(\lambda)$ is the spectral responsivity of the detectors (amps/W), $P(\lambda, \Theta)$ is the blackbody radiance, Eq. (2), and λ_{min} and λ_{max} are the lower and upper limits to the sensitivity of the detectors, respectively. Although it is difficult to determine ε and β with accuracy it is instructive to estimate these factors and to evaluate Eq. (4). Using $R(\lambda)$ for an InSb detector, provided by the detector manufacturer, $\varepsilon = .10$, $\beta = .57 \times 10^{-3}$, $A = 10^8$ V/A, $A_D = 2.5 \times 10^{-4}$ cm^2, the calculated $V(\Theta)$ relation is shown in Fig. 5.10. The figure shows that the $V(\Theta)$ relation is nearly linear in on a log-log plot. Also shown in Fig. 5.10 is the measured calibration [33] for a polished steel sample.

The measured calibration data were obtained by placing a heated sample of the material in front of the optical system and recording the sample temperature and voltage output of the detector as the sample cooled. Since the InSb detectors used do not respond to low-frequency signals, the radiation from the specimen must be chopped to give it a high-frequency component. This is done by placing a rotating disk with holes or slots in front of the detector. The radiation is chopped at 1 kHz, resulting in a 1 kHz square-wave output from the detector. The voltage recorded here is the peak to peak

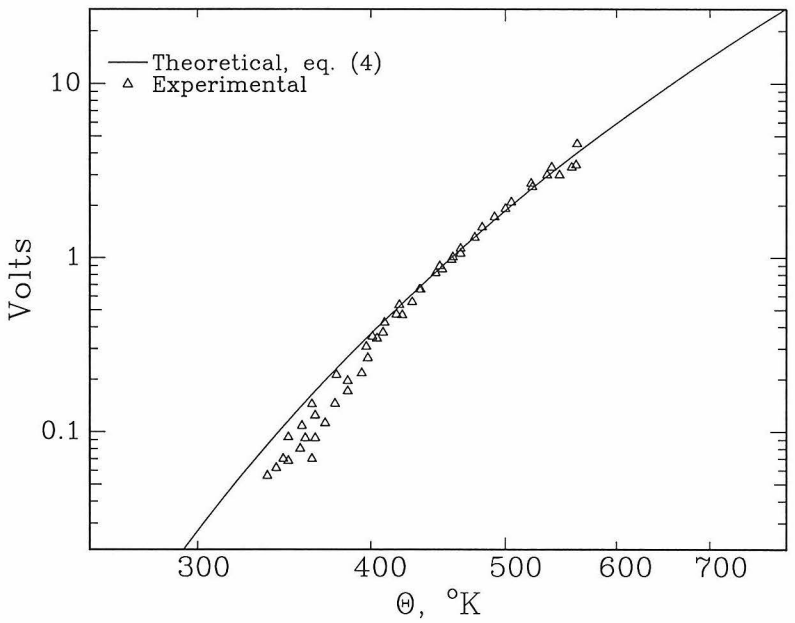

Figure 5.10. Theoretical calibration curve for an InSb detector and measured curve for a polished steels specimen [33]. ($\Theta_0 = 300$ K.)

voltage of the square-wave output. Although the theoretical and experimental calibrations are very similar to each other, they differ somewhat, indicating that the emissivity of the sample is not constant as assumed in evaluating Eq. (4).

Note also that during the calibration, the detector records the difference between the radiation emitted by the sample plus the background, and that emitted by the chopping wheel. Thus during calibration,

$$V_{\text{cal}}(\Theta, \Theta_0) = AA_D \int_{\lambda_{\min}}^{\lambda_{max}} R(\lambda)[\beta\varepsilon(\lambda, \Theta)P(\lambda, \Theta) + \varepsilon_B(\lambda, \Theta_0)P(\lambda, \Theta_0) - \varepsilon_{\text{CH}}(\lambda, \Theta_0)P(\lambda, \Theta_0)]\, d\lambda, \tag{5}$$

where ε_B is the effective emissivity of the background radiation and ε_{CH} is the emissivity of the chopping wheel. The first term in Eq. (5) is due to the radiation emitted from the sample, the second term is due to the background radiation (which is assumed to be chopped by the wheel), and the third term is due to the radiation from the chopping wheel. The voltage output corresponding to the background radiation can be experimentally determined by removing the calibration sample while spinning the chopping wheel and recording the voltage output. This voltage must then be subtracted from the calibration since in the actual experiment, the background radiation does not contribute to the signal. After subtracting the background voltage, the only difference between the $V(\Theta)$ relations of Eqs. (4) and (5) is

$$V - V_{cal} = AA_D \int_{\lambda_{min}}^{\lambda_{max}} R(\lambda)P(\lambda, \Theta_0)\,[\beta\varepsilon(\lambda, \Theta_0) - \varepsilon_{CH}(\lambda, \Theta_0)]\, d\lambda.$$

For InSb detectors, and assuming $\varepsilon_{CH} = 1$, $\Theta_0 = 293\ K$, the error introduced by ignoring this difference is negligible when $\Theta - \Theta_0 > 100\ K$, which is near the lower limit of sensitivity of the detectors. For detectors sensitive to longer wavelengths, where temperatures closer to ambient can be measured, the difference between the output obtained in a calibration, Eq. (5) and an experiment, Eq. (4), must be estimated and accounted for.

The emissivity of the sample is governed by the surface condition of the sample. Thus the surface finish of the calibration samples must be exactly the same as that of the actual test sample. When heating the calibration sample it may become heat tinted, affecting ε. This effect can be minimized by heating the calibration sample in an inert atmosphere or by lowering the temperature used for the calibration. This will limit the range of calibration. However, knowing the general form of the $V(\Theta)$ relation from the analytical calibration, one can extrapolate the experimental calibration beyond the range of measured temperatures.

Detector Cross Talk

In a multielement, semiconductor array, the individual elements are physically very close together and may thus affect each other, leading to "cross talk," where radiation incident on a detector element produces a small signal on the neighboring detector element. Errors in focusing will also produce an effective cross talk when radiation from a given region on the specimen is focused mostly on one detector element but with a fraction going to neighboring elements. Whatever the source of the cross talk, if a linear array of detector elements is being used, the cross talk can easily be measured and accounted for. To measure the cross talk, a wire of diameter less than the size of a single detector element, divided by the magnification of the optics, is placed in focus in place of the test specimen. The image of the wire is centered on one detector element by translating the wire until the signal observed from one detector is maximized. The ratio of the signal on elements adjacent to the central element provides a measure of the cross talk fraction. In many cases the cross talk will occur only on nearest neighbor elements.

To account for cross talk in processing the data, let s_i be the measured voltage on element i, and let r_i be the true signal at element i. We assume that

$$s_i = r_{i-1}\varphi + r_i + r_{i+1}\varphi, \tag{6}$$

where φ is the cross talk fraction. The above can then be written as a matrix equation for all elements and inverted to solve for the true signals, r_i. Note that when performing the calibration, $r_i = r$, thus $s_i = r(1 + 2\varphi)$. Consequently the calibration voltage should be divided by $(1 + 2\varphi)$.

Deconvolution of Data

Correcting for the cross talk is a type of deconvolution in the spatial dimension. In some cases deconvolution in the temporal dimension should be performed as well in order to recover the true signal. This is true when the maximum frequency content of the measured signal is close to the bandwidth of the detector. In this case the signal is spread out in time. An example [34] is shown in Fig. 5.11 where a step function of input radiation from an IR-LED results in a smooth ramp output from an InSb detector with $R_f = 10^6\ \Omega$. This process is described mathematically as a convolution,

$$V_{out}(t) = \int_{-\infty}^{\text{in}} V_{in}(\tau)h(t - \tau)d\tau, \tag{7}$$

where $h(t)$ is the impulse response, given for this particular example by Fig. 5.5. In an experiment, V_{out} is recorded, but V_{in} is what needs to be known. Thus V_{out} is deconvolved with $h(t)$ to find V_{in}. This is most easily performed using the fast Fourier transform, FFT. The FFT of V_{in} is given by

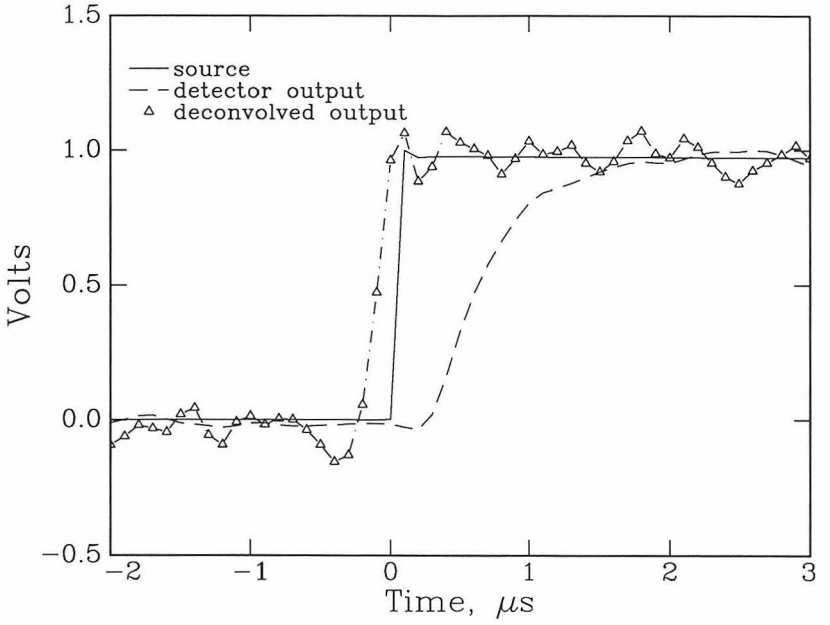

Figure 5.11. Response of an InSb detector with $R_f = 10^6\ \Omega$ to a step function radiation input, and deconvolved response.

$$\hat{V}_{in} = \hat{V}_{out}/\hat{h}$$

where the $\hat{V}$'s and $\hat{h}$ denote the the transforms. The transform $\hat{V}_{in}$ is then inverted to determine V_{in}. An example of a deconvolution for a detector with the impulse response given in Fig. 5.5 is shown in Fig. 5.11. It is seen that the deconvolution reproduces the input signal reasonably well.

If, as in the experiments described in the following section, you are measuring a moving temperature field with a stationary detector element, there is an additional convolution due to the finite size of the detector element. For example, if a step function wave of IR radiation moving at speed $\dot{a}$ crosses the detector element (with width D) the detector sees a ramp increase in the radiation as shown in Figs. 5.12(a) and 5.12(b). This ramp is then further convolved with the detector time response, $h(t)$, resulting in the measured signal shown in Fig. 5.12(c). The entire process is described mathematically as a double convolution

$$V_{in}(t) = V_{in}(x/\dot{a}),$$

$$V'(s) = \int_{-\infty}^{\infty} V_{in}(\tau)g(s - \tau)d\tau,$$

$$V_{out} = \int_{-\infty}^{\infty} V'(s)h(t - s)ds,$$

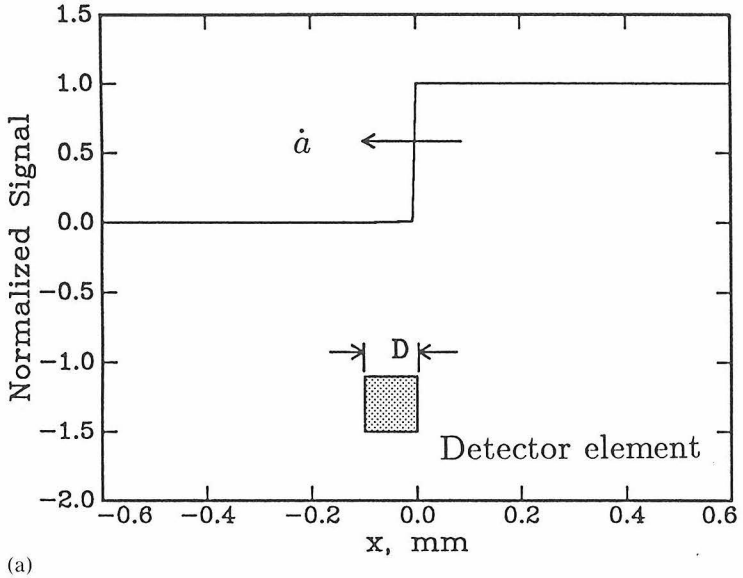

(a)

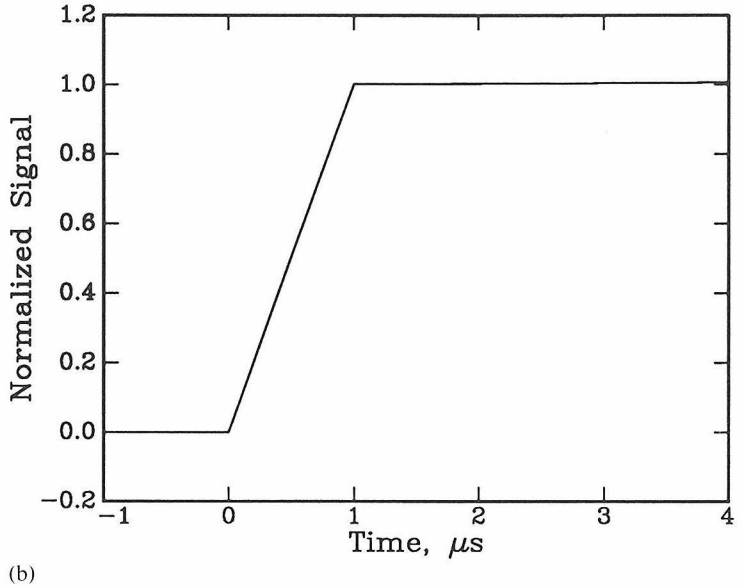

(b)

Figure 5.12. Response of IR detector element to a step function wave of IR radiation passing across the field of view of the detector. The example shown is for $D = 0.10$ mm, $\dot{a} = 0.10$ *mm*/μ*s*, and the impulse response $h(t)$ shown in Fig. 5.5. (a) Step function wave passing across the detector field of view. (b) Radiation seen by the detector. (c) Output signal from the detector is the convolution of 12b with the impulse response.

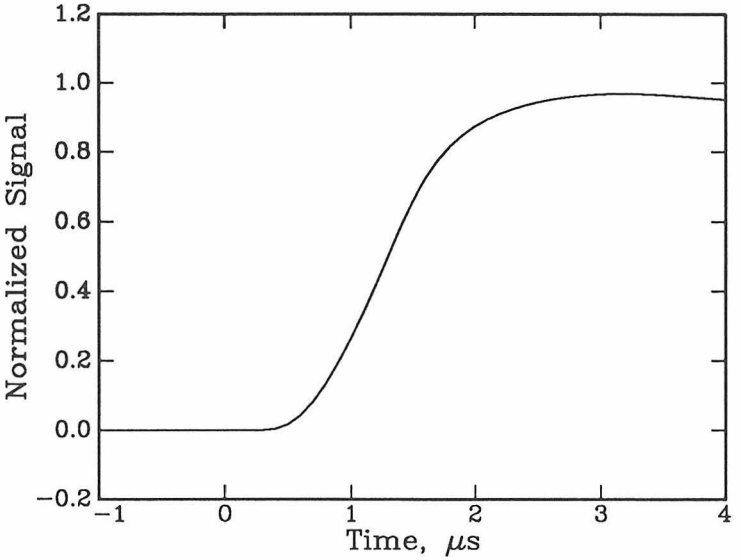

(c)

Figure 5.12. (*continued*)

where $g(t)$ is the geometric impulse response, given by the time derivative of the ramp shown in Fig. 5.12(b), i.e.,

$$g(t) = \begin{cases} 0, & \text{if } x \leq 0; \\ \dfrac{1}{(D/\dot{a})}, & \text{if } 0 < t \leq D/\dot{a}; \\ 0, & \text{if } t > D/\dot{a}. \end{cases}$$

Thus, to determine V_{in} from the measured V_{out} the double deconvolution

$$\hat{V}_{in} = \frac{\hat{V}_{out}}{\hat{g}\hat{h}},$$

is used.

Note that it is not necessary to use deconvolution in all cases. It is only needed when the measured signal is limited by the response of the detector. If the rise time of the measured signal is approximately equal to the rise time of the detector or to the rise time associated with the finite size of the detector element, then deconvolution should be used. However if the rise time of the measured signals is much longer than the detector rise times then deconvolution will not be needed.

Signal Processing Summary

The recommended processing for signals obtained from a linear array of detectors is to (1) eliminate the effects of cross talk for each time step, (2)

deconvolve the data for each detector element, and (3) use the calibration to convert voltage to temperature rise.

Application to Dynamic Crack Growth in 4340 Steel

A particular set of experiments [33] using an array of indium antimonide (InSb) detectors to measure the crack tip temperature rise in samples of 4340 steel is discussed here. In these experiments crack speeds ranged from 1200 to 600 m/s and the maximum temperature increase measured was 465 °C.

Test Specimens

The specimens used for this experiment were wedge-loaded compact tension specimens of 4340 steel with the dimensions shown in Fig. 5.13. The mechanical and thermal properties and chemical composition are given in Table 5.1. Note that two different heat treatments were tested in these experiments.

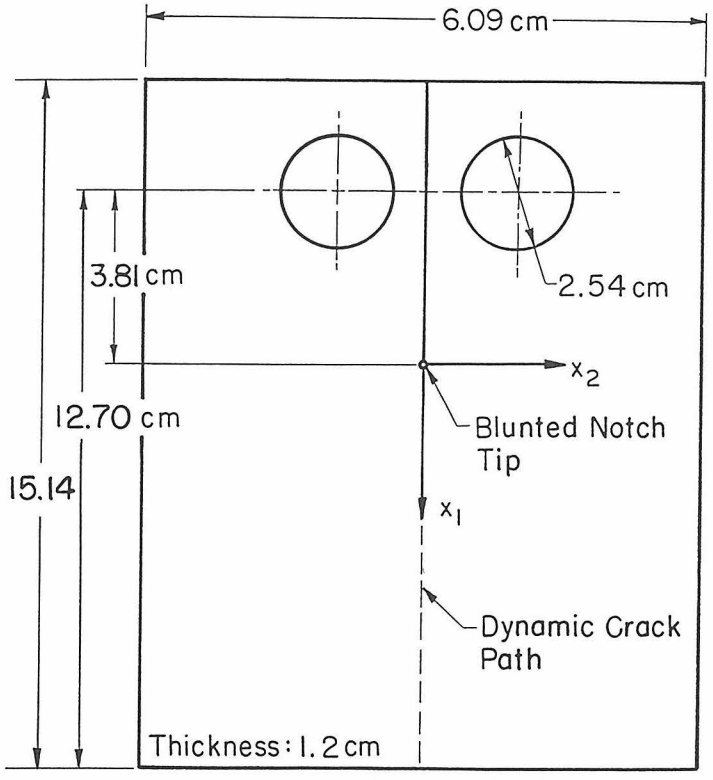

Figure 5.13. The wedge loaded compact tension specimen.

Table 5.1 MECHANICAL AND THERMAL PROPERTIES AND CHEMICAL COMPOSITION 4340 STEEL, AIRCRAFT QUALITY, VACUUM DEGASSED.

Heat Treatment	σ_0 (*MPa*)	K_{IC} ($MPa\sqrt{m}$)	Hardness (HRC)
"Quenched and tempered" 871 °C 1 hr., air cool 843 °C 1½ hr., oil quench 316 °C 1 hr., air cool	1490*	50*	44–45
"Oil quenched" 871 °C 1 hr., air cool 843 °C 1½ hr., oil quench	1700**	44**	49–55

Chemical Composition, %

C	Mn	P	S	Si	Cu	Ni	Cr	Mo	Sn	Al	Fe
.42	.71	.007	.013	.23	.12	1.78	.83	.25	.005	.033	Balance

Properties at 0 °C:**	
Thermal conductivity	$k = 34.6$ *W/m K*
Thermal expansion	$a = 11.2 \times 10^{-6}$ K^{-1}
Specific heat	$c = 448.0$ *J/kg K*
Density	$\rho = 7834$ kg/m^3
Thermal diffusivity	$\alpha = .99 \times 10^{-5}$ m^2/s

*Source: Zehnder and Rosakis [36].
**Source: *Aerospace Structural Metals Handbook*, Metals and Ceramics Information Center, Battelle Columbus Laboratories, Columbus, Ohio, 1989.

The wedge loaded compact tension geometry was chosen because the compressive stress parallel to the crack produced by the wedge stabilizes the crack path, ensuring straight crack growth. This was important in these experiments, since the detectors can measure across a distance of only 1.5 mm; thus the crack must propagate within .75 mm of the desired path in order for the experiment to be successful. The specimens were prepared by grinding, lapping, and then polishing the specimen surfaces with a 9 μm diamond paste. Several specimens had side grooves machined along the crack paths. Two geometries were used, a semicircular groove of radius 1.5 mm, and a *V*-notch groove of width 3 mm and depth 1.5 mm.

An array of lines of conductive paint spaced 3 mm apart was silk screened onto the back of each specimen, using techniques developed by Hudak et al. [35]. These strips are visible on the back of the specimen pictured in Fig. 5.14. As the crack runs, the conductive strips are broken and the resistance of the entire array is increased. Thus a time record of the resistance (measured with a bridge circuit) provides the time history of the crack motion. This technique has been shown to be very reliable for applications to high strength steel. The crack length record is differentiated using the incremental polynomial fit method [36]. Typical crack speed records are shown in Fig.

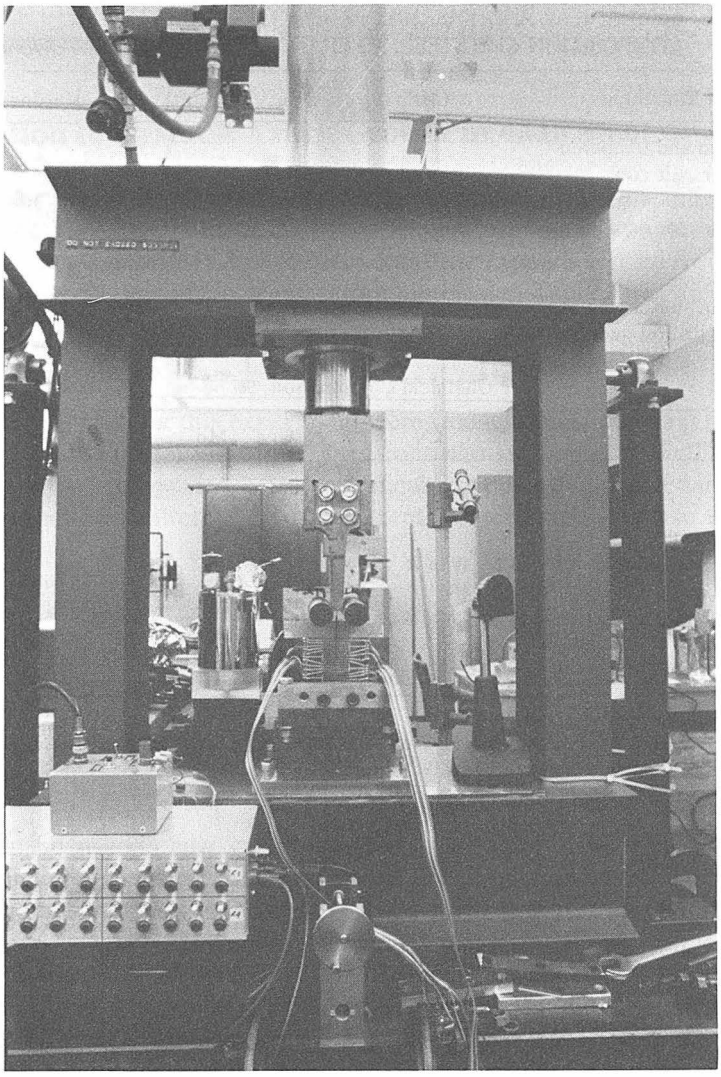

Figure 5.14. Photograph of loading frame mounted on optical table, loading wedge, test specimen, and conductive strips for crack speed measurement.

5.15 for oil quenched specimens containing an initial crack-tip diameter of 1 mm. It is seen that the crack speed $\dot{a}(a)$ is highly repeatable and remains nearly constant over a substantial portion of the specimen.

The specimens were loaded by a hydraulic cylinder mounted in a steel frame that rests on an optical table, as shown in Fig. 5.14. The wedge is driven slowly between the loading pins until a sharp crack initiates from the initially blunted notch tip. Due to the geometry of the loading and the initial

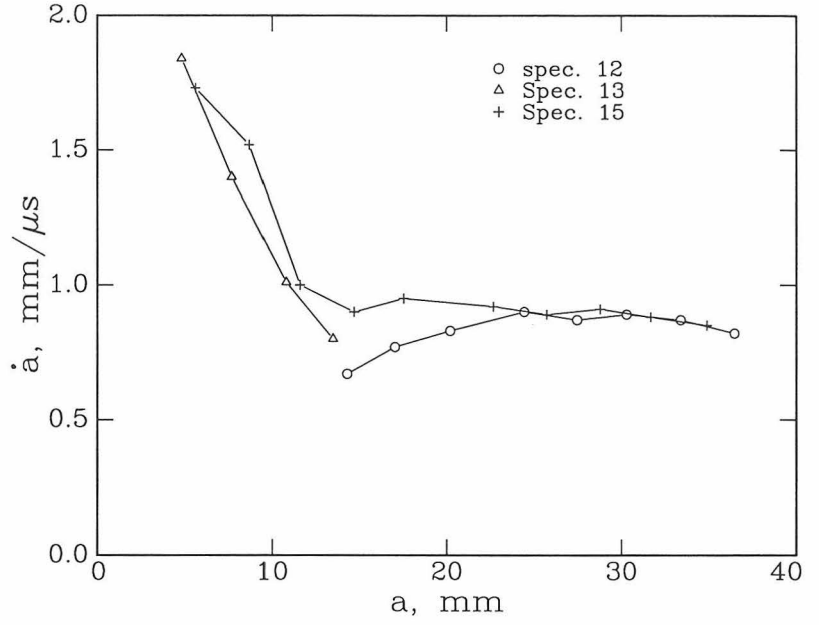

Figure 5.15. Crack speed versus crack length for oil quenched specimens.

bluntness of the notch, the resulting crack propagates unstably at high speeds ranging from 2000 to 1000 m/s, depending on the initial bluntness.

Infrared Detectors

Based on the analytical results summarized in the introduction, the maximum crack-tip temperature increases were anticipated to be in the range of 100–1000 °C. In addition, rise times for the temperatures were expected to be in the 1–2 μs range. At such temperatures the emitted infrared radiation is primarily in the 1–30μm wavelength range.

Our choice of indium antimonide (InSb), infrared (IR) detectors were dictated by the wavelength and rise time requirements described above. These detectors are sensitive to radiation with wavelengths from 1 to 5.5 μm. The particular system chosen was manufactured by Santa Barbara Research Center, and consists of eight .16 mm × .16 mm InSb detector elements in a linear array with a center to center spacing of 0.20 mm. The array is mounted in a liquid nitrogen (LN2) dewar to cool the detectors to 77 K, thus minimizing their electrical noise and maximizing their sensitivity. The LN2 dewar is clearly visible in the photograph of Fig. 5.16 and is sketched in Fig. 5.17. The detectors are located behind the sapphire window in the dewar.

Each detector is connected to its own amplifier and the amplified signals are recorded on separate high-speed digital oscilloscopes, at a 2 MHz sam-

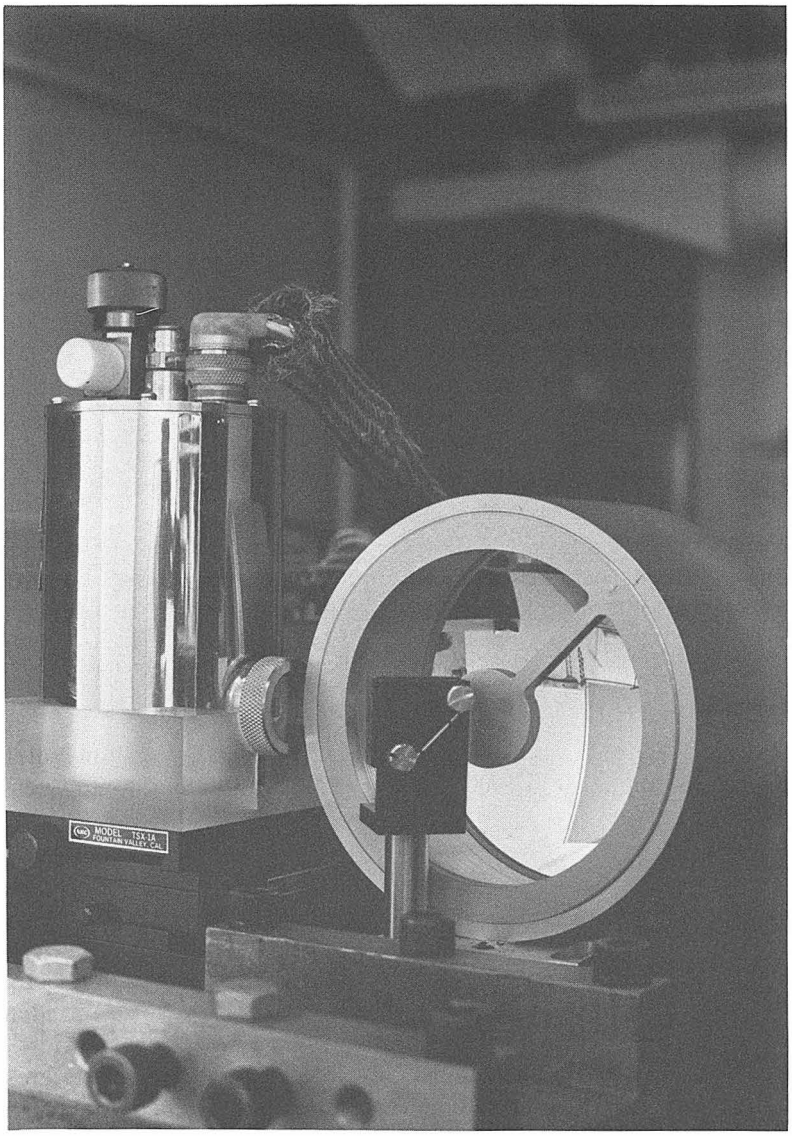

Figure 5.16. Photograph of IR detector dewar and mirrors.

pling rate. The frequency response of the system of detectors and their amplifiers is from 4 Hz to 300 kHz. The 4 Hz lower limit means that the system is not affected by low-frequency background radiation. The 300 kHz upper limit corresponds to a minimum detectable rise time of .75 μs, well below the anticipated 1–2 μs rise times.

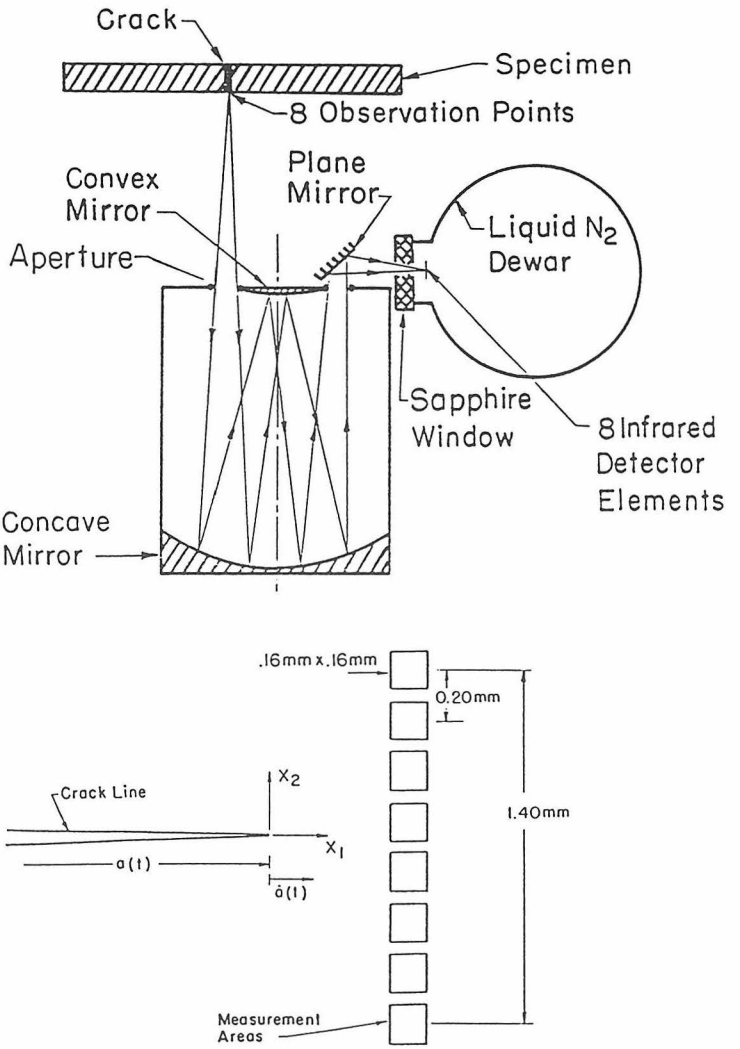

Figure 5.17. Schematic of focusing optics and of points on the test specimen from which temperature is measured.

The responsivity of the system used here is on the order of 10^8 V/W, and the maximum output signal is approximately 15 V. In order to avoid saturating the system, the amount of radiation incident on the detectors was limited by placing a small aperture in the optical system.

It was found that temperature increases as low as 20 °C could be detected. However, when the temperature increase was less than approximately 50 °C, the signal-to-noise ratio was on the order of 1. Thus accurate data could not be obtained from surfaces at temperatures below 50 °C above ambient.

Infrared Optics

To measure the crack-tip temperature distribution, the infrared radiation must be imaged from eight areas on the specimen surface onto eight elements of the detector array. The optical system, illustrated in Fig. 5.17, and also seen in Fig. 5.16, is the Offner system discussed previously. The magnification of the optical system is one, and thus the size and spacing of the areas of measurement are equal to that of the detectors. As shown in Fig. 5.17, the size of the measurement areas is 160 $\times$ 160 μm, the center-to-center spacing is 200 μm while the total length of the array from end to end is 1.56 mm. The system is aligned so that the eight measurement regions on the specimen surface are situated on a line segment perpendicular to and intersecting the crack path, as sketched in Fig. 5.17.

Initial optical alignment was performed by installing a Plexiglass replica of the actual specimen in the specimen holder. A laser beam was aimed through the Plexiglass replica, perpendicular to the replica surface and passing through the region on the specimen where it is desired to measure the temperature. The optical system was adjusted so that the laser beam passed perpendicularly through the center of the aperture and onto the center of the detectors. To aid in focusing, a 10 lines/mm crossed diffraction grating was taped onto the replica and the grating was illuminated. Fine focusing was performed by adjusting the optics until the image of the grating on the detector elements was sharp.

To align the detectors such that they intersect the prospective crack lines, a .10 mm-diam wire was carefully taped to the specimen along the prospective crack path. The specimen was then put in place in the loading frame. The wire was electrically heated and the system was aligned so that the radiation from the wire was sensed on one of the central elements.

The heated wire has a diameter less than the size of the detector elements, thus ideally, radiation from the wire should be detected on one element only and not on the neighboring elements. However, crosstalk that is intrinsic to the closely spaced detector array and is also due to optical aberrations will produce a small signal on the neighboring elements. It was found that the crosstalk was approximately 7%. The procedure discussed previously, Eq. (6), was used to account for the cross talk.

Calibration

Careful calibration is crucial for obtaining accurate results. As discussed previously, the procedure was to heat a sample of the 4340 steel, with the same surface finish as the actual test specimens, in a furnace. When the heated sample was removed from the furnace, it was placed in front of the optical system such that it is in focus. As the sample cools the voltage output from the detectors and the sample temperature (measured with a thermocouple) were simultaneously recorded. The radiation was chopped at

1 kHz by placing a rotating disk containing holes around its perimeter into the optical path. The resulting calibration is shown in Fig. 5.10.

Note that separate calibrations were performed for the notched specimens since inside the notches the surface finish and hence the emissivity was different. Roughening of the specimen surface at the crack tip will also change the emissivity. This effect was investigated by Hartley, Duffy, and Hawley [13], who showed that it is negligible for most of the temperature range.

Results

Figure 5.18 shows the time record of the voltage output of each of the eight detector elements, as a crack approaches and passes through the detector points in specimen number 9. Time $t = 0$ corresponds to the triggering of the oscilloscopes. The material used in this experiment was an oil quenched 4340 steel whose material characteristics appear in Table 5.1. For this experiment and for this particular measurement location, the crack-tip speed was found to be approximately constant and equal to 900 m/s (see the right-hand section of Fig. 5.15). The maximum voltage increase was recorded by element 4 (Ch4 in the figure). As is clear from the time record corresponding to this channel, the voltage increases rapidly from an almost zero value (from

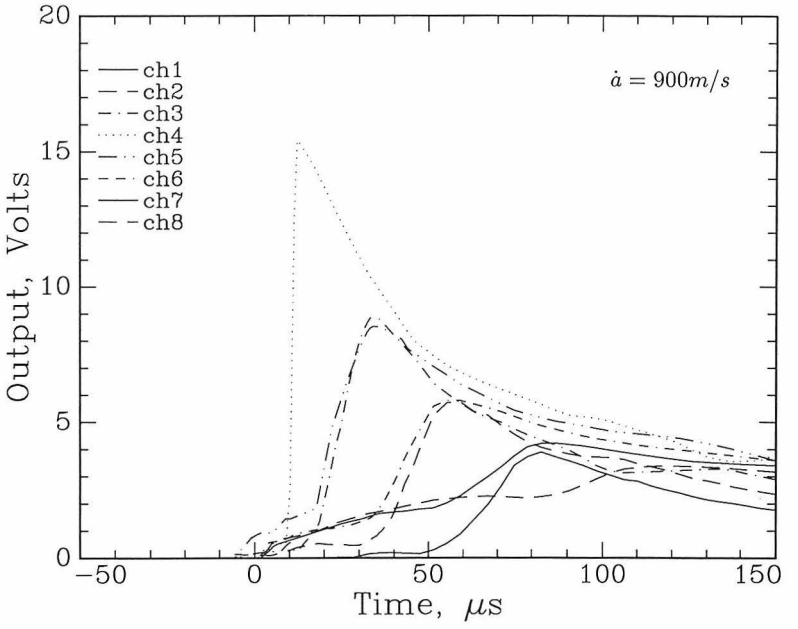

Figure 5.18. Specimen 9, oil quenched steel, IR detector output. Voltage versus time for each element.

within the noise level of the system) to a maximum value of 16.5 V in approximately 2 μs. This rise time is substantially longer than the limit of 0.75 μs which is the minimum rise time that can be accurately detected by the detector-amplifier unit of our measuring system.

The voltage output time histories were converted into temperature histories by means of the calibration relation shown in Fig. 5.10. Since this relation is nonlinear, the resulting temperature records, shown here in Fig. 5.19, assume a slightly different shape than the voltage records, but nevertheless retain the basic characteristic forms of Fig. 5.18. In this experiment the crack tip traversed the array of detection points slightly off center, but through the region focused on element 4. This element recorded a maximum temperature increase of 450 °C while the rise time was 2 μs. As it may be expected by local symmetry, the elements to the left and right of element 4 (channels 3 and 5) recorded temperature increases which are very similar to each other. These elements also had markedly slower rise times than element 4.

Two alternative ways of viewing these results are shown in Figs. 5.20 and 5.21. These figures show contours of equal temperature *increase*, $T \equiv \Theta - \Theta_0$, near the propagating crack-tip. The contours were obtained from the temperature increase versus time results of Fig. 5.19, by converting the time axis into distance parallel to the direction of crack growth, using the mea-

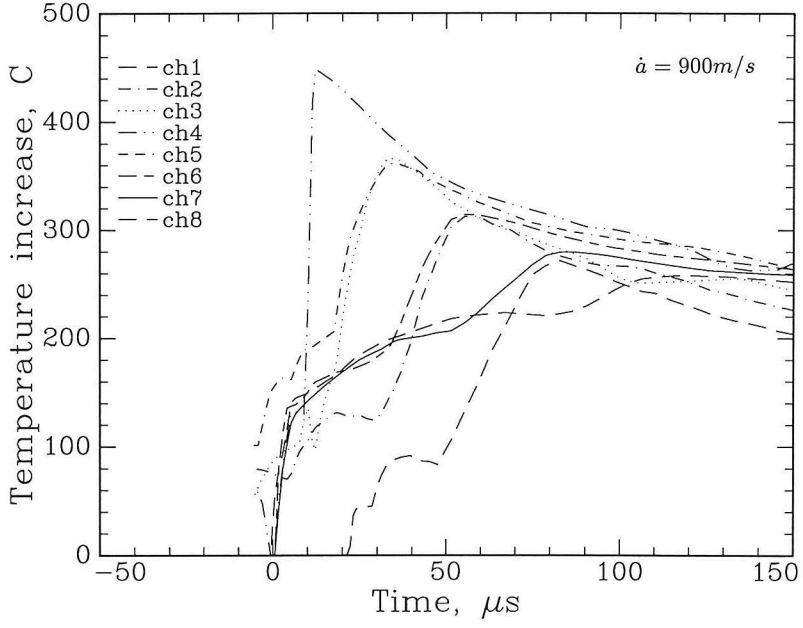

Figure 5.19. Specimen 9, temperature increase over ambient versus time for each detector element.

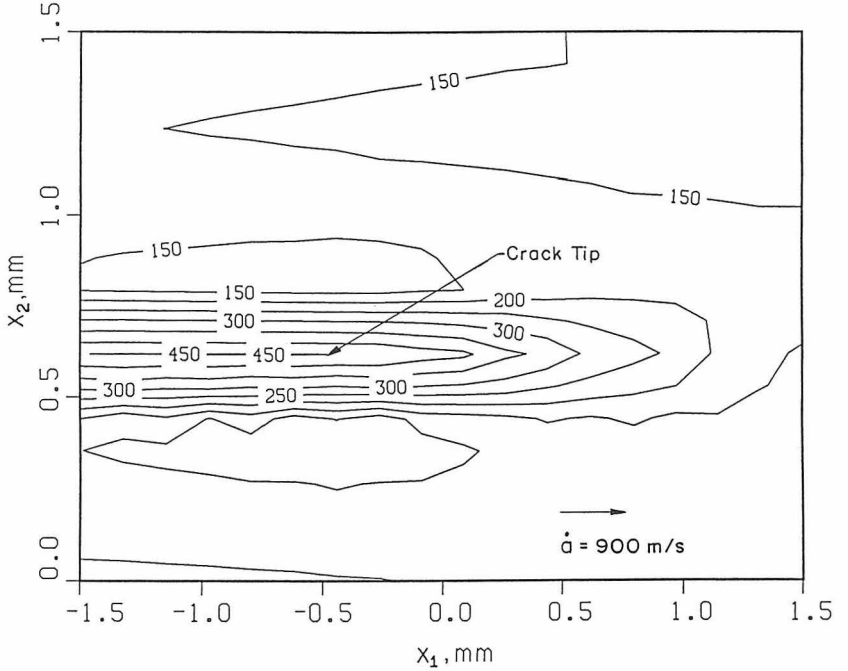

Figure 5.20. Specimen 9, contours of equal temperature rise very near the crack-tip. Increment between contours is 50 °C.

sured crack tip speed of 900 m/s and assuming that the crack propagates with a constant velocity. Although this is clearly a simplifying assumption, its appropriateness is justified by the velocity history data presented in Fig. 5.15 at least for observation distances greater than 12 mm from the tip of the initial notch.

In both Figs. 5.20 and 5.21 the estimated crack-tip position is at $x_1 \simeq -0.5$ *mm*, $x_2 \simeq 0.6$ *mm*. The length scales of Fig. 5.20 show that this figure corresponds to a *close-up* view of temperature increase in the near vicinity of the propagating crack. The isotherms of Fig. 5.20 clearly show that intense heating (temperatures ranging from 450 to 150 °C) extends in a narrow region approximately 1 mm ahead of the crack tip, while the half width of the resulting wake of temperatures is approximately 0.25 mm. It should be observed that the isotherms in the wake region behind the crack-tip remain almost parallel to the crack line for at least 1.5 mm, suggesting that *locally*, the deformation remains essentially adiabatic (i.e., no substantial cooling by conduction is observed in this local scale.).

The scale of observation of Fig. 5.21 is very different. Here we present contours of temperature increase for distances behind the crack-tip as large as 60 mm.

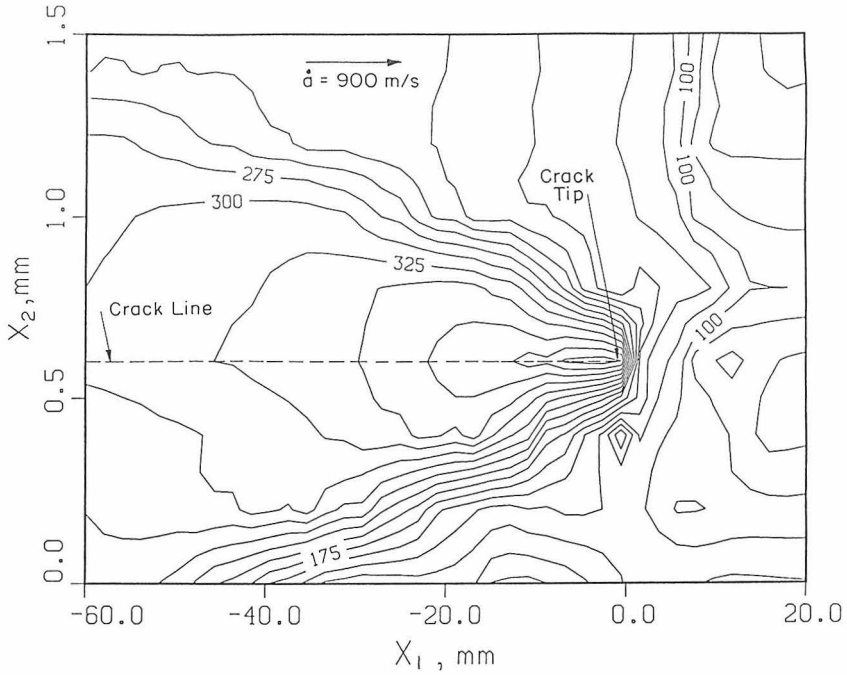

Figure 5.21. Specimen 9, contours of temperature increase in the region away from the crack-tip.

It should be re-emphasized perhaps at this point that the measurements are performed over small but nevertheless finite areas (see Fig. 5.17) and that the above contours have been obtained by assigning the recorded temperature history to the center of these areas. It should therefore be recognized that a certain amount of averaging is involved in this measurement. Nevertheless it is expected that the small size areas allow for the accurate investigation of the general structure of the temperature distribution near the tip. On the other hand, this unavoidable averaging makes the recorded *maximum* temperature increase a lower bound to the actual maximum temperature increase at the crack-tip.

Figures 5.22 and 5.23 show contours of equal temperature increase at the vicinity of a crack in an oil quenched and tempered 4340 steel specimen. The crack-tip velocity was 980 m/s and the crack traversed the array of observation points off center. Comparison between Figs. 5.20 and 5.22, and 5.21 and 5.23, show a very similar structure in temperature distribution for these two heat treatments. Comparison between all the experiments conducted on the oil quenched and the oil quenched and tempered steels reveals only slight differences in maximum temperature increases for similar velocity. The general trend observed is that maximum temperatures corresponding to the more brittle oil-quenched steel are up to 10 °C higher than those recorded for the quenched and tempered heat treatment.

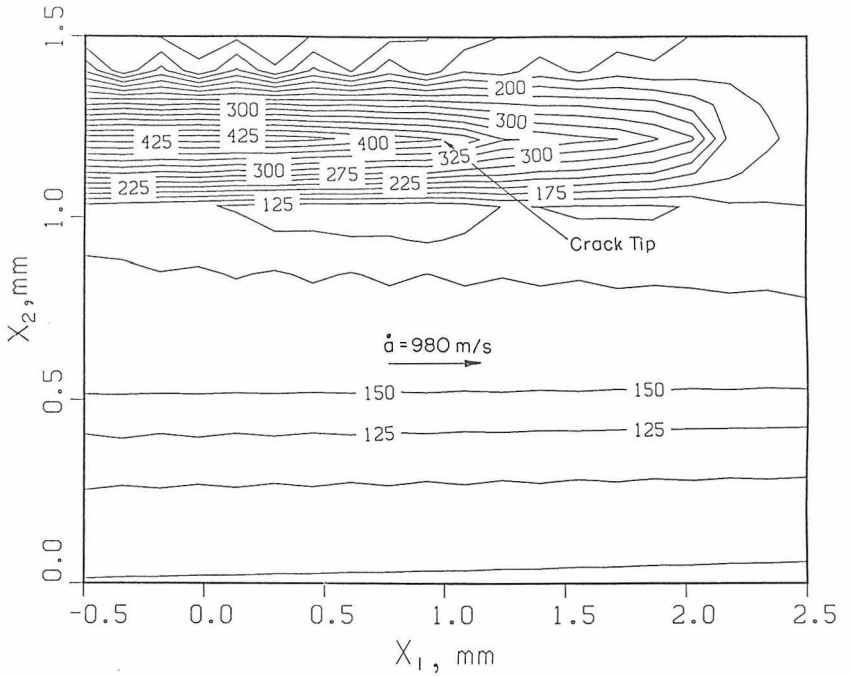

Figure 5.22. Specimen 5 (quenched and tempered steel), contours of temperature increase near the crack-tip.

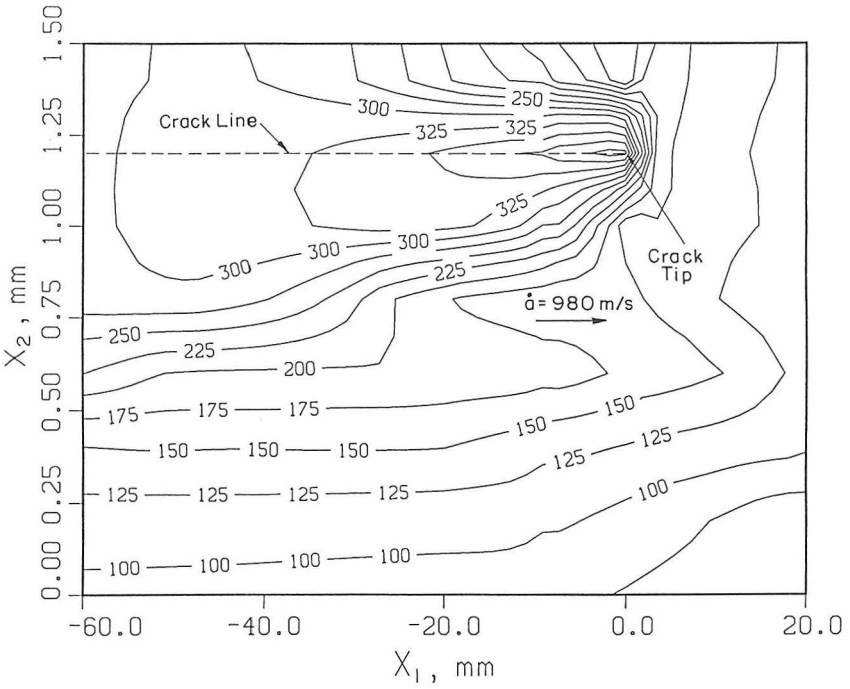

Figure 5.23. Specimen 5, contours of temperature increase in the region away from the crack-tip.

Effects of Shear-Lip Formation on Temperature

In the experimental results of Fig. 5.20, the crack traversed the array of observation points near the center. This was not always possible to achieve given the net length of the array of observation points (total length of 1.56 mm perpendicular to the prospective crack path) and the fact that it was not always possible to create a perfectly straight crack to within such a small tolerance.

Figure 5.24(a) shows the spatial distribution of temperature for the case of a crack that traversed the array of observation points near the array end. In this case (specimen 12) the maximum temperature increase was recorded by the end element, number 8, located at $x_2 = 1.4$ mm in the figure. This element shows the most dramatic increase of temperature ahead of the tip and records a temperature peak of 415 °C. Perhaps the most interesting feature of this figure is the ridge of local temperature increase shown along the line $x_2 = 0$, furthest away from the crack line. This local temperature increase occurs at points approximately 1.4 mm away from the crack line and was consistently observed in a number of experiments.

The existence of a local maximum in temperature always occurring at a consistent distance away from the crack line is explained if one takes a close look at the fracture surface of the specimen shown in Fig. 5.25. The photograph clearly reveals a flat fracture surface in the specimen interior while a well formed shear lip is evident near the specimen surface. The wake of residual plastic deformations is also shown on the specimen surface in the form of a strip of out of plane deformation (local dimpling) along the crack path. The width of this strip was found to be approximately equal to 1.4 mm, which is slightly smaller than the net length of our line of observation points. In addition, the width of this strip is equal to the distance between the crack and the ridge of temperature increase shown in Fig. 5.24. This is illustrated in the schematic of Fig. 5.26. This figure shows a thickness cross section of the specimen, the crack lip as well as the shear lips near the specimen surface. The eight dots that appear on the specimen surface represent the eight temperature measurement locations. In the specimen interior the crack surface is flat and lies on the plane $x_2 = 0$ while on the specimen surface shear lips are shown.

The process of the creation of shear lips involves some amount of crack-tip tunneling followed by the formation of two symmetric 45° shear bands (solid and dotted lines), one of which ruptures (solid line) to produce the 45° crack observed on the specimen surface. The major peak of temperature increase (see Fig. 5.24) corresponds to the tip of the crack while the minor peak lies exactly at the location where the 45° shear band (dotted line) meets the specimen surface.

Further evidence of the existence of the ridge of temperatures associated with the 45° shear band is given in the experimental result shown in Fig. 5.27. In this experiment the infrared system was focused slightly off center to investigate this heating due to the formation of the shear band alone. The

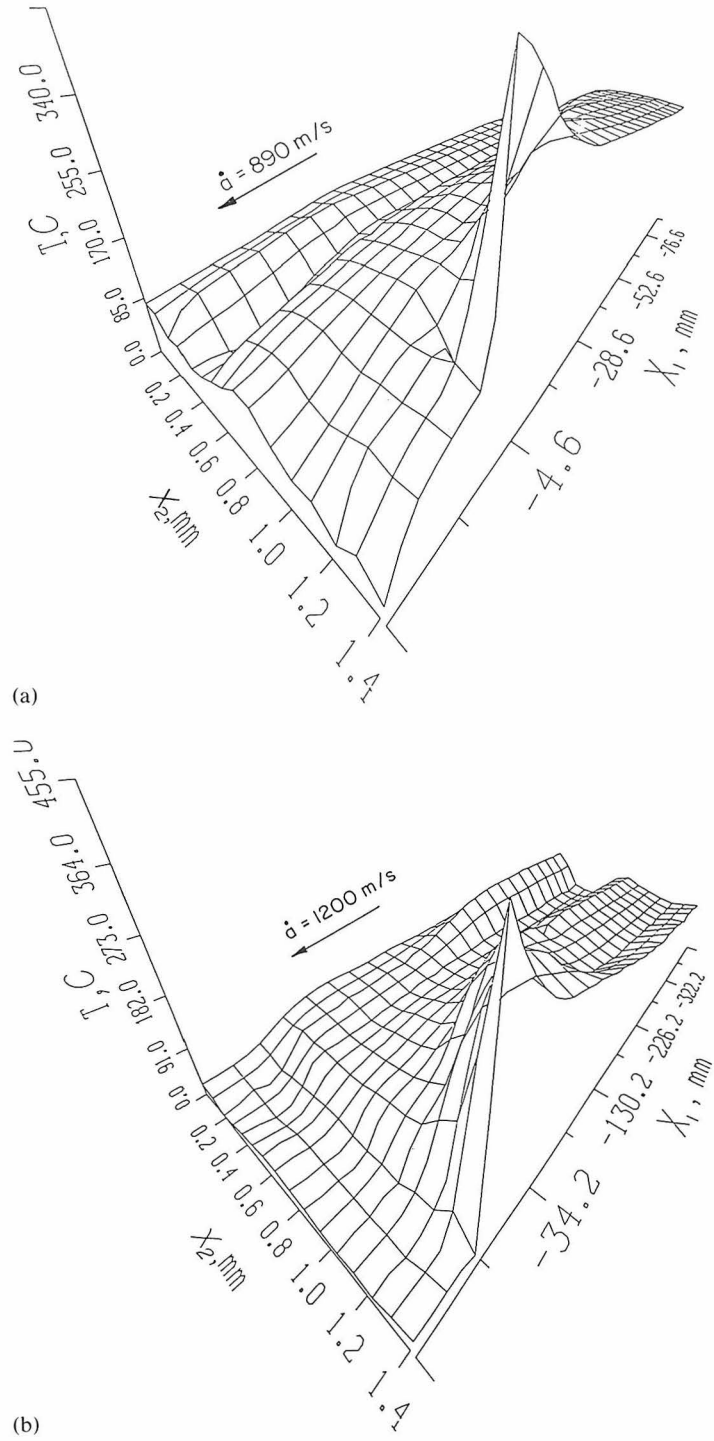

Figure 5.24. Surface plots of temperature increase showing major peak due to crack-tip and secondary peak due to the 45° shear band corresponding to the opposite side of the shear lips. (a) Specimen 12. (b) Specimen 17.

Figure 5.25. Photograph of fracture surface and shear lips.

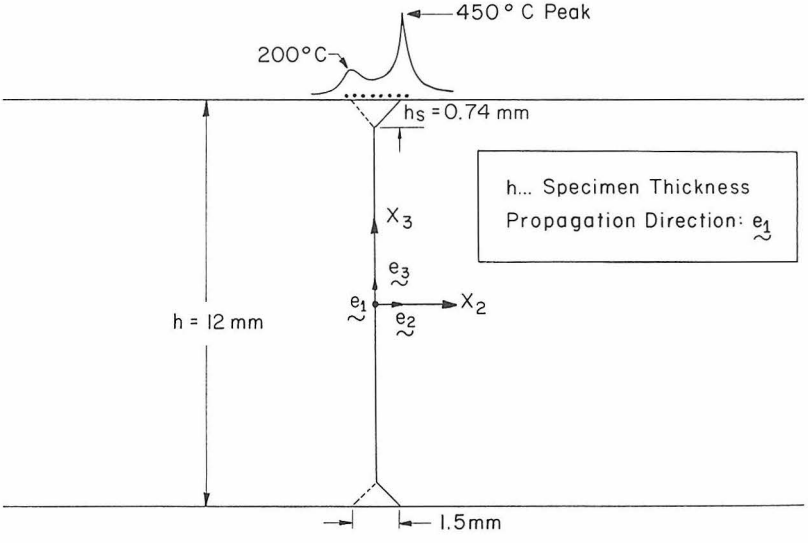

Figure 5.26. Schematic of the thickness cross section of the specimen illustrating the formation of shear lips and the associated temperature distribution on the free surface.

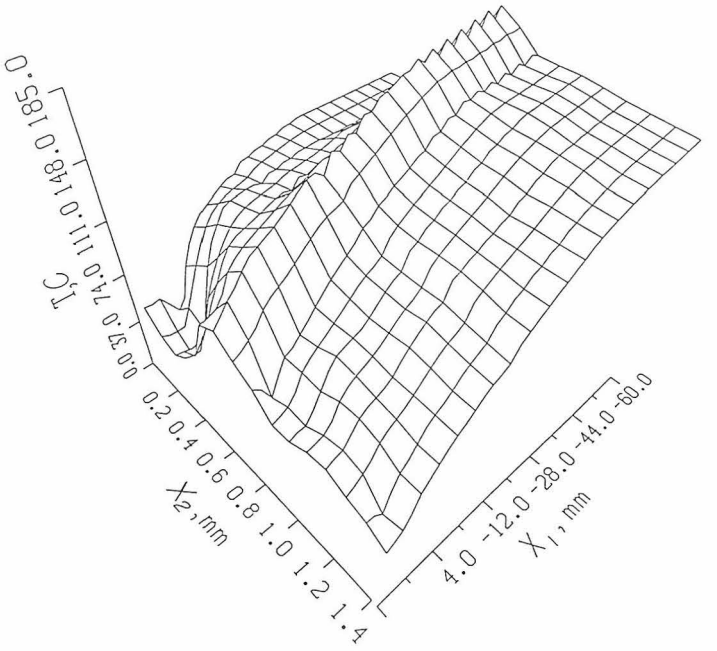

Figure 5.27. Specimen 7, surface plot of temperature showing the ridge of temperature due the opposite side of the shear lip.

temperature increase recorded here is on the order of 200 °C and is well above the noise level of our recording system. Figures 5.24 and 5.27 show that the temperature measurements accurately reflect the highly three-dimensional nature of the rupture process on the specimen surface.

Finally, it should be emphasized here that the temperature measurements described above strictly reflect the structure of the temperature fields on the specimen surface. The very short time scales involved in this measurement ensure that conduction from the specimen interior has no time to affect the temperature recorded on the surface at the vicinity of the dynamically propagating crack. A simple calculation based on known values for the thermal conductivity of 4340 steel reveals that at the time scales of this measurement, the temperature on the specimen surface is only affected by points of the interior lying within distances of less than 30 μm below the specimen surface. In addition, the time scales involved preclude the possibility of any cooling effects due to convection or net radiation losses during dynamic growth.

Specimens with Side Grooves

The results presented in the previous section provide a very accurate account of the spatial structure of the temperature field on the specimen sur-

face. These temperature increases are strongly dominated by the complex process of the dynamic formation of shear lips which involves the simultaneous formation of dynamic shear bands and cracks intersecting the surface at 45°. However, in order to obtain some idea of the temperature rise in the specimen's interior, a preliminary series of experiments was performed in which the specimen surfaces were side grooved. The side grooving was designed to diminish the effect of shear lips and to provide conditions that would at least approximate plane strain like crack-tip field constraints in the specimen interior. Two sets of side grooves of v notched and circularly notched geometries were machined along the prospective crack paths. Figure 5.28 shows a set of temperature time records corresponding to specimen number 5.24. These measurements are conducted by focussing the eight detector elements inside the side grooves. A separate calibration was performed to account for the difference in surface roughness due to the machining of the grooves. Due to the small aperture used, the large depth of field of the optical system allows us to focus simultaneously at any level inside the side groove. Our preliminary experiments (see Table 5.2) indicate that the use of side grooves diminishes the size of the resulting shear lips and in addition results in peak temperatures which are up to 20% lower than

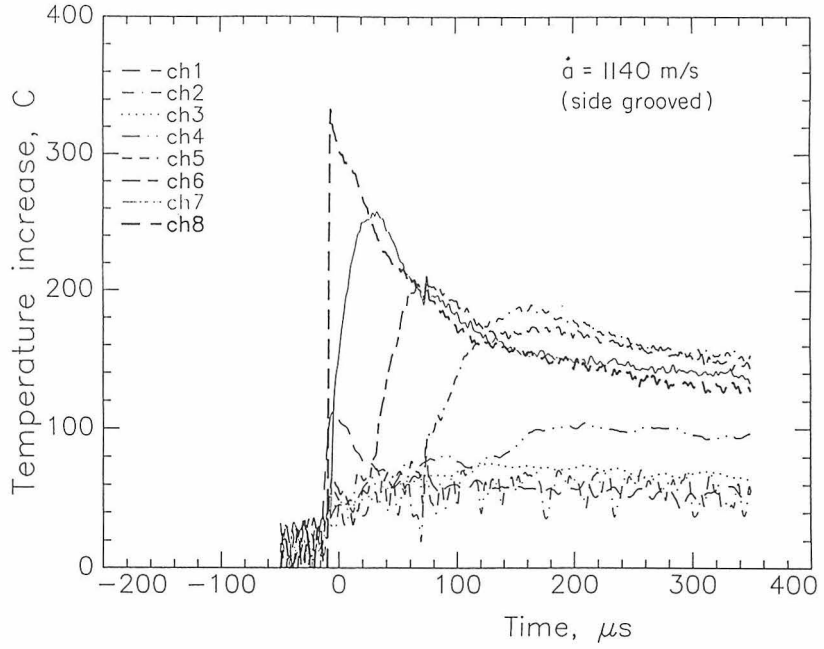

Figure 5.28. Specimen 24 (circular groove), temperature rise versus time for each detector element.

Table 5.2 SUMMARY OF EXPERIMENTS.

Specimen	Heat Treatment	a (*mm*)	$\dot{a}$ (*m/s*)	T_{max} (°C)	Notes
1	tempered	29	730	410	
5	tempered	29	980	415	
7	oil quenched	14	950	185	shear band temperature
9	oil quenched	14	900	450	
12	oil quenched	25	890	425	
13	oil quenched	8	1300	410	
17	oil quenched	8	1200	465	focused in circular groove
21	oil quenched	8	1100	≥420	Voltage went off scale
22	tempered	8	1900	290	focused in *V*-notch
24	tempered	8	1140	330	focused in circular groove

those recorded by the corresponding measurements of the specimen surface. This reduction may be attributed to differences in the near tip constraints between notched and unnotched geometries.

Discussion of Results

Plastic Work Rate

The distribution of plastic work rate near the crack-tip can be obtained by straightforward differentiation of the temperature field. Assuming that the heating due to plastic work is much higher than the thermoelastic effects and treating the crack growth as steady state, Eq. (1) can be written as

$$k\nabla^2\Theta + \eta\sigma_{ij}\dot{\varepsilon}^P_{ij} = -\rho c\dot{a}\frac{\partial\Theta}{\partial x_1}, \tag{8}$$

with respect to a coordinate system translating where x_1 is the direction of crack growth. Note that the conduction term with the crack-tip, $k\nabla^2\Theta$, in Eq. (8), involves derivatives of Θ with respect to x_3, while the measurement provides only $\Theta(x_1, x_2, x_3 = h/2)$ where h is the specimen thickness. The very short time scales of this measurement (2–10 μs) ensure that convection and radiation heat losses from the surface are very small. In addition, as discussed in the introduction, conduction of heat from the interior of the specimen has no time to affect the surface temperatures near the crack tip. As a result, the variation of Θ with respect to x_3 is expected to be small, and little error is incurred by neglecting the $\partial^2\Theta/\partial x_3^2$ in Eq. (8). Indeed when differentiating $\Theta(x_1, x_2, x_3 = h/2)$ the entire conduction term was found to be small relative to the adiabatic heating term $-\rho c\dot{a}\partial\Theta/\partial x_1$. For distances from

the crack-tip of less than 2 mm, the ratio $\rho c \dot{a} \partial \Theta / \partial x_1 / k \nabla^2 T$ was approximately 10^3, while for distances greater than 20 mm the ratio was approximately 10^1.

The plastic work rate, $W^P(x_1, x_2) = \sigma_{ij} \dot{\pi}^P_{ij}$, was obtained for all specimens assuming $\eta = 0.9$ in Eq. (8). Typical results are presented in Figs. 5.29 and 5.30 which show the plastic work rate distribution for specimen 9. Figure 5.29 shows the contours of plastic work rate. The maximum value of the plastic work rate was $400 \times 10^{12}\ J/m^3 - s$. It is seen that the region of the active plastic zone ($\dot{W}^P > 0$) lies just ahead of the crack-tip and is elongated in the x_1 direction. This elongation was unexpected and must be related to the way the fracture meets the specimen surface along a 45° angle (see Fig. 5.25). The distribution is very symmetric for this particular experiment. Note that in differentiating experimental data unavoidable numerical errors are introduced, hence little significance should be attributed to very low values of $\dot{W}^P$ that are below the noise level of the differentiation process which is of the order of $20 \times 10^{12}\ J/m^3 - s$. The peak of $\dot{W}^P$ which lies ahead of the crack-tip is clearly seen in Fig. 5.30 where $\dot{W}^P$ is plotted three dimensionally. This figure shows that, except for a few oscillations, $\dot{W}^P$ is essentially 0 everywhere except in a region just ahead of the crack-tip.

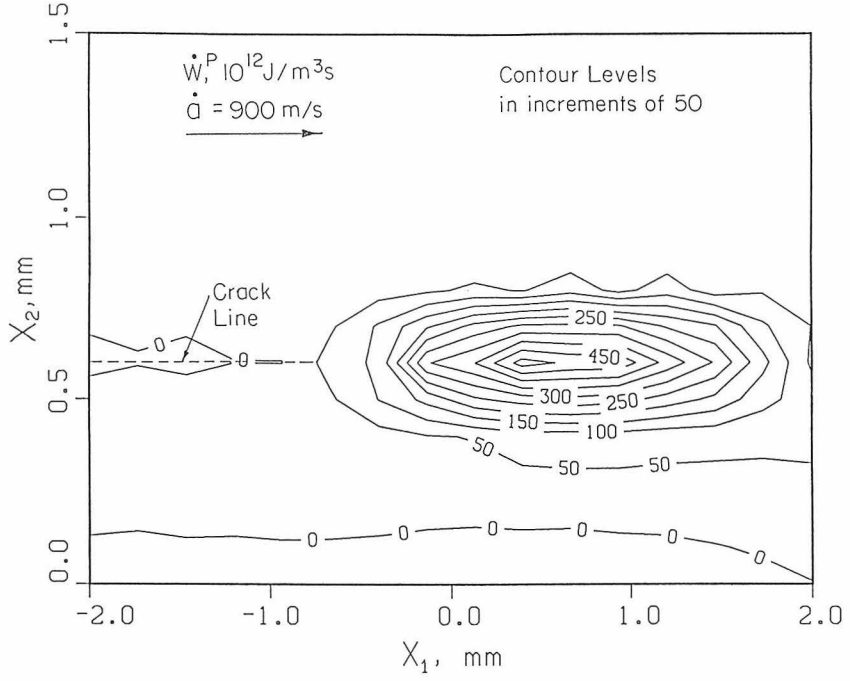

Figure 5.29. Specimen 9, contours of plastic work density near the crack tip. Increment between contours is $50 = \times 10^{12}\ J/m^3\ s$.

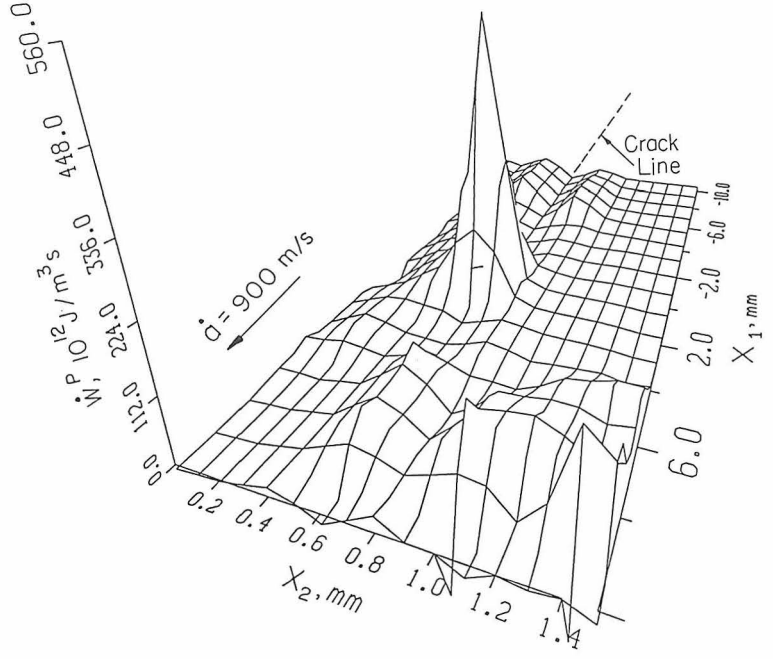

Figure 5.30. Specimen 9, surface plot of plastic work density.

A rough estimate of the maximum plastic strain rate may be obtained from a simple calculation that assumes a von Mises yield criterion with a constant yield stress σ_0 equal to the static value given in Table 5.1 for the quenched and tempered steel. In this case

$$\| \dot{\epsilon}^P_{ij}(\tilde{x}) \| = \frac{\dot{W}^P(\tilde{x})}{\sigma_0} \sqrt{\frac{3}{2}}. \tag{9}$$

By using the maximum value of the plastic work rate, $\dot{W}^P_{max} = 400 \times 10^{12}\ J/m^3 - s$, Eq. (9) gives maximum strain rate $\| \dot{\epsilon}^P_{ij} \|_{\max} \simeq 5 \times 10^5\ s^{-1}$.

Comparison to analytical results

The temperature contours obtained here are very similar in shape to those calculated by Weichert and Schönert [37] and Kuang and Atluri [7]. However, the values of temperature are quite different and cannot be compared since their calculation is intended to model brittle fracture where a high temperature localized over a very small region is expected. Rice and Levy [5] modeled crack growth in elastic-plastic, rate insensitive materials and give an analytical relation for the maximum crack-tip temperature rise which in-

volves K_I, σ_0, $\dot{a}$, and the thermal properties of the material. During crack growth K_I^d can be assumed to be equal to the dynamic fracture toughness K_{Ic}^d of the material. For the quenched and tempered 4340 steel, the K_{IC}^d versus $\dot{a}$ relationship can be inferred from the experimental results of Zehnder and Rosakis [36]. For specimen 5 $\dot{a}$ = 980 m/s and $K_{IC}^d \approx 120$ MPa$\sqrt{\text{m}}$. Using these values, the thermal properties given in Table 5.1, and σ_0 = 1490 *MPa*, a temperature increase of 3,800 °C is predicted. Although the peak measured temperatures are lower than the actual temperatures due to the averaging effect of the detector size, clearly the actual temperature rise is much lower than predicted. This is to be expected [5], since the Dugdale model used for the calculation lumps all of the deformation and hence all of the heating onto a single line.

Role of Heating on Fracture Toughness

The experimental data show that temperature increases up to 465 °C may occur at the tip of dynamically propagating cracks in 4340 steel. Such large temperature increases may have a significant effect on dynamic fracture propagation toughness.

Three interacting phenomena that might be affected by local crack-tip heating are outlined below. These are the decrease in yield stress at higher temperatures, the change in the fracture mechanism, and the change in the local structure of the near-tip fields.

Data from the *Metals Handbook* [38] on yield stress versus temperature for the tempered 4340 steel indicate that the yield stress in tension at 450 °C is 50% lower than that at room temperature. Dislocation motion is thermally activated and will be affected by local crack-tip heating even of the time scales of this process, since there is no delay time associated with the effect temperature increase on mobility. As a result, near the crack-tip there is a possibility of a substantial decrease of yield stress due to local heating.

A reduced yield stress near the crack-tip will cause a change in the crack-tip stress and strain fields compared to the fields that would exist under isothermal conditions. If crack growth is governed by a local criterion such as the attainment of a critical strain or opening angle at some distance near the crack-tip, the effect of temperature on the local deformation fields will affect the fracture toughness of the material. It is not clear whether such effects will enhance or degrade fracture toughness. In general, lower yield stress values are associated with higher fracture toughness. Although this is true for a limited temperature range, this cannot be extrapolated indefinitely, since in the limit as the temperature approaches the melting point, both σ_0 and the fracture toughness must eventually approach 0.

Data of Chi et al. [39] show that dynamic fracture initiation toughness for the tempered 4340 steel at 100 °C is 50% higher than at room temperature. Care must be taken in extrapolating this data to apply to dynamic fracture

propagation toughness since in performing high-temperature fracture *initiation* tests the material will be held at a high temperature for some time, causing a certain amount of heat treating of the material to occur. However, in dynamic crack growth experiments there is insufficient time for any diffusion of atoms to take place and thus no heat treating can occur.

In an attempt to predict fracture toughness for dynamic crack growth, isothermal models use fracture criteria implemented very near the crack-tip. It is exactly in such regions where the experimental data show temperature rises as high as 400 °C. In light of the above observation, it appears that thermal effects should be incorporated in such models.

Summary

Application of high-speed IR detectors to dynamic deformation and failure experiments is an exciting development in experimental mechanics. Although only a few years old the method is already providing results in fracture, shear band formation and other fields. Coupled with analytical and numerical analyses that account for heat generation and coupling of constitutive models and temperature, this method promises to widely expand our capability to understand dynamic deformation and failure processes.

Acknowledgments

This work was begun at Caltech with the support of the ONR, through Contract Nos. N00014-85-K-0596 and N00014-90-J-1340 and has continued both at Caltech and at Cornell, with support at Cornell from NSF, Contract No. MSS-8910000 the ONR, Contract No. N00014-89-J-3184, and the Materials Science Center at Cornell, NSF/MSC-DMR-8818558. The assistance of Mr. Jacob Kallivayalil is also gratefully acknowledged.

References

1. Taylor, G.I. and Quinney, M.A., "The Latent Heat Remaining in a Metal After Cold Work," *Proc. R. Soc. London Ser. A* vol. 143, 307–326 (1934).
2. Bever, M.B., Holt, D.L., and Titchener, A.L., *The Stored Energy of Cold Work, Prog. Mater. Sci.* Vol. 17 (1973).
3. Zehnder, A.T., "A Model for the Heating due to Plastic Work," *Mech. Res. Com.* Vol. 18, pp. 23–28 (1991).
4. Carslaw, H.S. and Jaeger, J.C., *Conduction of Heat in Solids* Clarendon Press Oxford (1959).

5. Rice, J.R. and Levy, N., "Local Heating by Plastic Deformation at a Crack Tip," in *The Physics of Strength and Plasticity,* edited by A.S. Argon (MIT Press, Cambridge, MA, 1969), pp. 277–292.

6. Weichert, R. and Schönert, K., "Heat Generation at the Tip of a Moving Crack," *J. Mech. Phy. Solids* Vol. 22, 127–133 (1978).

7. Kuang, Z.-B. and Atluri, S., "Temperature Field due to a Moving Heat Source: A Moving Mesh Finite Element Analysis," *J. Appl. Mech.* Vol. 52, 274–280 (1985).

8. Malali, P.N., "Thermal Fields Generated by Dynamic Mode III Fracture in Ductile Metals," M.S. Thesis, The Johns Hopkins University, Baltimore, Maryland (1988).

9. Krishnakumar, R., Narasimhan, R., and Prabhakar, O., "Temperature Rise in a Viscoplastic Material During Dynamic Crack Growth," Indian Inst. of Tech., Bombay, Rep # ARDB-STR-TR8951901.

10. Needleman, A. and Tvergaard, V., "An Analysis of Dynamic Crack Growth in a Double Edge Cracked Specimen," Brown University Report, August 1989.

11. Rosakis, A.J. and Deng, X. "Dynamic Crack Propagation in Elastic Plastic Solids under Plane Stress Conditions" *J. Mech. Phy. Sol.,* Vol. 39, 683–722 (1991).

12. Moss, G.L. and Pond, R.B., "Inhomogeneous Thermal Changes in Copper During Plastic Elongation," *Metallurg. Trans. A* Vol. 6A, 1223–1235 (1975).

13. Hartley, K.A., Duffy, J., and Hawley, R.H., "Measurement of the Temperature Profile During Shear Band Formation in Steels Deforming at High Strain Rates," *J. Mech. Phys. Solids* Vol. 35, 283–301 (1987).

14. Crisman, E.E., Duffy, J., and Chi, Y.C., "A Short Rise Time Probe for Temperature Measurements During the Formation of Dynamic Shear Bands," in *Micromechanics: Experimental Techniques,* ASME AMD, Vol. 102, edited by W.N. Sharpe, (American Society of Mechanical Engineers, New York, 1989), pp. 163–178.

15. Monchalin, J.-P. and Bussière, J.F., "Measurement of Near-Surface Ultrasonic Absorption by Thermo-Emissivity," in *Nondestructive Methods for Material Property Determination,* edited by C.O. Ruud and R.E. Greed (Plenum Press, New York 1984), pp. 289–297.

16. Baker, L.R. and Oliver, D.E., "Full Field Stress Analysis Using the Thermoelastic Principle," *Proceedings Infrared Tech. XII,* Society for Photooptical Instrumentation Eng. (SPIE) Vol. 685, 23–28, Bellingham, WA (1986).

17. Fuller, K.N.G., Fox, P.G., and Field, J.E., "The Temperature Rise at the Tip of Fast Moving Cracks in Glassy Polymers," *Proc. R. Soc. London Ser. A.* Vol. 341, 537–557 (1975).

18. Shockey, D.A., Kalthoff, J.F., Klemm, S., and Winkler, S., "Simultaneous Measurements of Stress Intensity and Toughness for Fast Running Cracks in Steel," *Exp. Mech.* Vol. 40, 140–152 (1983).

19. Döll, W., "An Experimental Study of the Heat Generated in the Plastic Region of a Running Crack in Different Polymeric Materials," *Eng. Fract. Mech.* Vol. 5, 259–268 (1973).

20. Tomashevskii, E.E., Egorov, E.A., and Sovodstin, A., Ya., "Thermal Effects During Fracture in Polymers," *Int. J. Fract.* Vol. 11, 817–827 (1975).

21. Fox, P.G. and Soria-Ruiz, J. "Fracture-Induced Thermal Decomposition in Brittle Crystalline Solids, *Proc. R. Soc. London Ser. A* Vol. 317, 79–90 (1970).

22. Kobayashi, A., Munemura, M., Ohtani, N., and Suemasu, H., "Estimation of Heat Evolution During Viscoelastic Crack Propagation by Liquid Crystal Film Technique," *J. Appl. Polymer Sci.* Vol. 27, 3763–3768 (1982).

23. Bryant, J.D., Makel, D.D., and Wilsdorf, H.G.F., "Observations of the Effect of Temperature Rise at Fracture in Two Titanium Alloys," *Mater. Sci. Eng.* Vol. 27, 85–93 (1986).

24. Klemm, W., presented at the Joint American Society of Mechanical Engineers, Japan Society of Mechanical Engineers International Pressure Vessels and Piping Conference, July 1989.

25. Wong, A.K. and Kirby, G.C.III, "Determination of the heat Dissipated from a Specimen Undergoing Cyclic Plasticity by a Hybrid Numerical/Experimental Method," NRL Memorandum Report 6633, May, 1990.

26. Beghi, M.G., Bottani, C.E., Caglioti, G., and Lenti, A., "Energy Balance via Thermal Emission in Copper Under Stress," *Mater. Lett.* Vol. 6, 133–137 (1988).

27. *Semiconductors and Semimetals*, Willardson, R.K. and Beer, A.C. ed's Vol. 5 of *Infrared Detectors* (Academic Press, New York, 1970).

28. Wolfe, W.L. and Zissis, G.J., Eds., *The Infrared Handbook* (Environmental Research Institute of Michigan, 1978) Ann Arbor Mich.

29. Infrared Optical Products Inc., Optics for the Infrared Catalog, Farmingdale, NY.

30. Offner, A., "New Concepts in Projection Mask Aligners," *Opt. Eng.* Vol. 14, 130–132 (1975).

31. Ealing Electro-Optics Corp., South Natick, MA, 1990 Catalog.

32. Kingslake, R., *Lens Design Fundamentals*, (Academic Press, New York 1978).

33. Zehnder, A.T. and Rosakis, A.J., "On the Temperature Distribution at the Vicinity of Dynamically Propagating Cracks in 4340 Steel: Experimental Measurements Using High Speed Infrared Detectors." *J. Mech. Phys. Solids* Vol. 39, 385–417, (1991).

34. Kallivayalil, J. A. and Zehnder, A.T. "Measurement of the Temperature Field Induced by Dynamic Crack Growth in Beta-C Titanium," submitted to *International Journal of Fracture*, 1993.

35. Hudak, S.J., Dexter, R.D., Aaron, V.D., and Nagy, A., "Techniques for Measuring Displacements and Crack Growth During Dynamic Fracture," Southwest Research Institute internal report (1987).

36. Zehnder, A.T. and Rosakis, A.J., "Dynamic Fracture Initiation and Propagation in 4340 Steel Under Impact Loading," *Int. J. Fract.* Vol. 43, 271–285 (1990).

37. Weichert, R. and Schönert, K., "On the Temperature Rise at the Tip of a Fast Running Crack," *J. Mech. Phys. Solids* Vol. 22, 127–133 (1974).

38. *Metals Handbook, Properties and Selection: Irons and Steels* (American Society for Metals, Metals Park, OH 1978).

39. Chi. Y.C., Lee, H.S., Cho, K., and Duffy, J., "The Effects of Tempering Temperature and Test Temperature on the Dynamic Fracture Initiation of AISI 4340 VAR Steel," *Mater. Sci. Eng.* Vol. A114, 105–126 (1989).